Received: 22 February 2022 | Revised: 16 May 2022 | Accepted: 19 May 2022

DOI: 10.1111/jmg.12683

ORIGINAL ARTICLE

Journal of METAMORPHIC GEOLOGY WILEY

Multi-episodic formation of baddeleyite and zircon in polymetamorphic anorthosite and rutile-bearing ilmenitite from the Chiapas Massif Complex, Mexico

Alejandro Cisneros de León[1,2] | **Axel K. Schmitt**[1] | **Bodo Weber**[3]

[1]Institute of Earth Sciences, Heidelberg University, Heidelberg, Germany

[2]School of the Earth, Ocean and Environment, University of South Carolina, Columbia, South Carolina, USA

[3]Departamento de Geología, Centro de Investigación Científica y de Educación Superior de Ensenada (CICESE), Ensenada, Mexico

Correspondence
Alejandro Cisneros de León, School of the Earth, Ocean and Environment, University of South Carolina, 701 Sumter Street, EWS 617, Columbia, SC 29208, USA.
Email: acisneros@seoe.sc.edu

Funding information
Consejo Nacional de Ciencia y Tecnología (CONACYT), Grant/Award Number: CB-2016-01-285638; Deutsche Forschungsgemeinschaft (DFG), Grant/Award Number: SCHM 2521/4-1

Handling Editor: Prof. Clare Warren

Abstract

Massif-type anorthosite and comagmatic associations of rutile-bearing ilmenitite (RBI) and oxide-apatite-rich amphibolite (OARA) from the Chiapas Massif Complex (CMC) in southeastern Mexico display a protracted billion-year accessory mineral record encompassing magmatic crystallization at c. 1.0 Ga to recent ductile shear deformation at c. 3.0 Ma. Multiple discrete zircon populations between these age end-members resulted from neoformation/recrystallization during local to regional metamorphism that affected the southeastern portion of the CMC. The ubiquitous presence of relict baddeleyite (ZrO_2), along with various zircon generations spatially associated with pristine to partly retrogressed Zr-bearing igneous and metamorphic minerals (e.g., ilmenite, rutile, högbomite and garnet), suggests significant Zr diffusive re-equilibration (exsolution) during slow cooling and mineral breakdown followed by crystallization of baddeleyite. The subsequent transformation of baddeleyite into zircon was likely driven by reaction with Si-bearing fluids in several geochronologically identified metamorphic stages. Strikingly contrasting compositional signatures in coeval zircon from anorthosite (silicate-dominated) and comagmatic RBI (Ti-Fe-oxide-dominated) indicate a major role of fluids locally equilibrating with the rock matrix, as indicated by distinct zircon trace element and oxygen isotopic compositions. A high-grade metamorphic event at c. 950 Ma is likely responsible for the formation of coarse-grained rutile (~0.1–10 mm in diameter), srilankite, zircon and garnet with rutile inclusions as well as metamorphic högbomite surrounding Fe-Mg spinel. Zr-in-rutile minimum temperatures suggest >730°C for this event, which may correlate to rutile-forming granulite facies metamorphism in other Grenvillian-aged basement rocks in Mexico and northern South America. A younger generation of baddeleyite exsolution occurred during post-peak cooling of coarse-grained rutile, reflected in rimward Zr depletion and formation of discontinuous baddeleyite coronas. Baddeleyite around rutile was then

transformed into zircon possibly during subsequent metamorphism at c. 920 or 620 Ma, resulting from syn-kinematic and contact metamorphism, respectively. Regional metamorphism at c. 450 and 250 Ma extensively overprinted the existing zircon population, especially during the Triassic event, as suggested by a significant presence of zircon with this age. Nearly pristine baddeleyite occurring interstitial to ilmenite yielded an isochron age of c. 232 Ma according to in situ U–Pb secondary ion mass spectrometry (SIMS), suggesting either formation during metamorphic peak conditions or post-peak cooling. Zircon with ages of c. 80–100 Ma in anorthosite is identified for the first time within the CMC and coincides with cooling ages of c. 100 Ma for coarse-grained rutile. This age is similar to those of rocks occurring ~200 km further to the east in Guatemala, which are also bounded to the Polochic fault system but overprinted by eclogite facies metamorphism. A high-pressure event in the southern CMC after 200 Ma, however, is presently unsupported. Although the abundance of rutile and ilmenite is unusually high in the CMC anorthosite assemblage compared with common igneous rocks, the reactions documented here nonetheless stress the importance of these phases for generating Zr-bearing accessory minerals over a wide range of metamorphic conditions.

KEYWORDS
Diffusion, SIMS, Srilankite, Ti-Fe deposits, Ti-in-zircon, Zr-in-rutile

1 | INTRODUCTION

Although mafic igneous rocks rarely bear primary zircon, it commonly emerges as an accessory component after metamorphism (Beckman et al., 2014; Harley et al., 2007). The Zr sources for the crystallization of neoformed zircon have been linked either to protolith-inherited zircon itself (protocryst) or to the release of Zr resulting from exsolution processes or breakdown reactions from magmatic or metamorphic Zr-bearing minerals (e.g., baddeleyite, ilmenite, rutile, garnet and amphibole; Austrheim et al., 2008; Bea et al., 2006; Beckman & Möller, 2018; Beckman et al., 2014, 2017; Bingen et al., 2001; Charlier et al., 2007; Cisneros de León et al., 2017; Davidson & Van Breemen, 1988; Degeling et al., 2001; Fraser et al., 1997; Kohn et al., 2015; Morisset & Scoates, 2008; Naslund, 1987; Pujol-Solà et al., 2020; Sláma et al., 2007; Söderlund et al., 2004, 2008). While the mechanisms of protocryst zircon recrystallization are relatively well understood (Hoskin & Black, 2000), the origins of neoformed zircon after Zr-bearing parental minerals remain unclear, especially due to the lack of textural evidence preserving arrested zircon-forming reactions. The precise understanding of the timing, conditions and mechanisms of zircon formation in meta-mafic rocks is essential to chronicle metamorphic histories and constrain geological interpretations (Beckman et al., 2017; Bingen et al., 2001; Degeling et al., 2001; Fraser et al., 1997; Harley et al., 2007; Sláma et al., 2007). Insights into timescales or temperatures not directly recorded by zircon can be gleaned from baddeleyite (U–Pb) and rutile (U–Pb and Zr-in-rutile), which provide complementing geochronological and thermochronological information (Ferry & Watson, 2007; Schmitt et al., 2010; Schmitt & Zack, 2012).

The southeastern part of the Chiapas Massif Complex (CMC) in southeastern Mexico, also referred to as the El Triunfo Complex (Weber et al., 2018, 2020), is a polymetamorphic complex with a history spanning c. 1.0 Ga that includes intrusion of Proterozoic massif-type anorthosite and related Ti-Fe oxide deposits experiencing at least five well-documented tectonothermal events (Cisneros de León et al., 2017; González-Guzmán et al., 2016; Valencia-Morales et al., 2022; Weber et al., 2007, 2018, 2020). Anorthosites and related rocks in the CMC preserve an outstanding zircon age and textural record defined by multiple zircon age populations, coincident in some cases with known regional and local metamorphic episodes (Cisneros de León et al., 2017; Weber et al., 2020). Petrographic analysis has revealed complex textures of zircon populations in anorthosite and their associated rocks (Cisneros de León et al., 2017). Here, we follow up on these initial observations by documenting textures, mineralogical context, ages and compositions of zircon and other accessory minerals from anorthosite and

cogenetic oxide-apatite-rich amphibolite and Ti-Fe oxide lenses. While anorthosite and oxide-apatite-rich amphibolite preserve no evidence of zircon-forming reactions (e.g., baddeleyite relicts in zircon) in grains associated with Ti-Fe oxides, comagmatic rutile-bearing ilmenitite (RBI) exhibit a wide spectrum of textures attesting to arrested zircon-forming reactions. This provides an unrivalled opportunity to identify mechanisms and conditions of recrystallization and neoformation of metamorphic zircon in mafic rocks and to establish links between the timing of zircon crystallization and reactions involving Zr-bearing minerals. For this purpose, we present a detailed petrographical study combined with new U–Pb zircon ages as well as trace elements (including Ti-in-zircon temperatures) and O isotope compositions determined by secondary ion mass spectrometry (SIMS). Additionally, co-existing rutile and baddeleyite were also dated by SIMS, and rutile was subjected to Zr-in-rutile thermometry by electron microprobe (EMP) analysis. EMP compositions of minerals that are potential Zr-repositories were also acquired.

2 | THEORETICAL BACKGROUND

2.1 | Geological setting

Anorthosite and associated rocks (RBI, hornblendite, oxide-apatite-rich amphibolite and nelsonite) are among the oldest basement units within the ~20,000 km^2 CMC in southeasternmost Mexico (Maya Block; Figure 1; Cisneros de León et al., 2017; Weber et al., 2018, 2020). Their likely age of c. 1.01 Ga is inferred from spatially associated granitic gneisses (Weber et al., 2018) and depleted-mantle Nd model ages (1.39–1.45 Ga; Cisneros de León et al., 2017) that are similar to those of Late Mesoproterozoic anorthosite-mangerite-charnockite suites elsewhere in Mexico (AMCG; e.g., Pluma

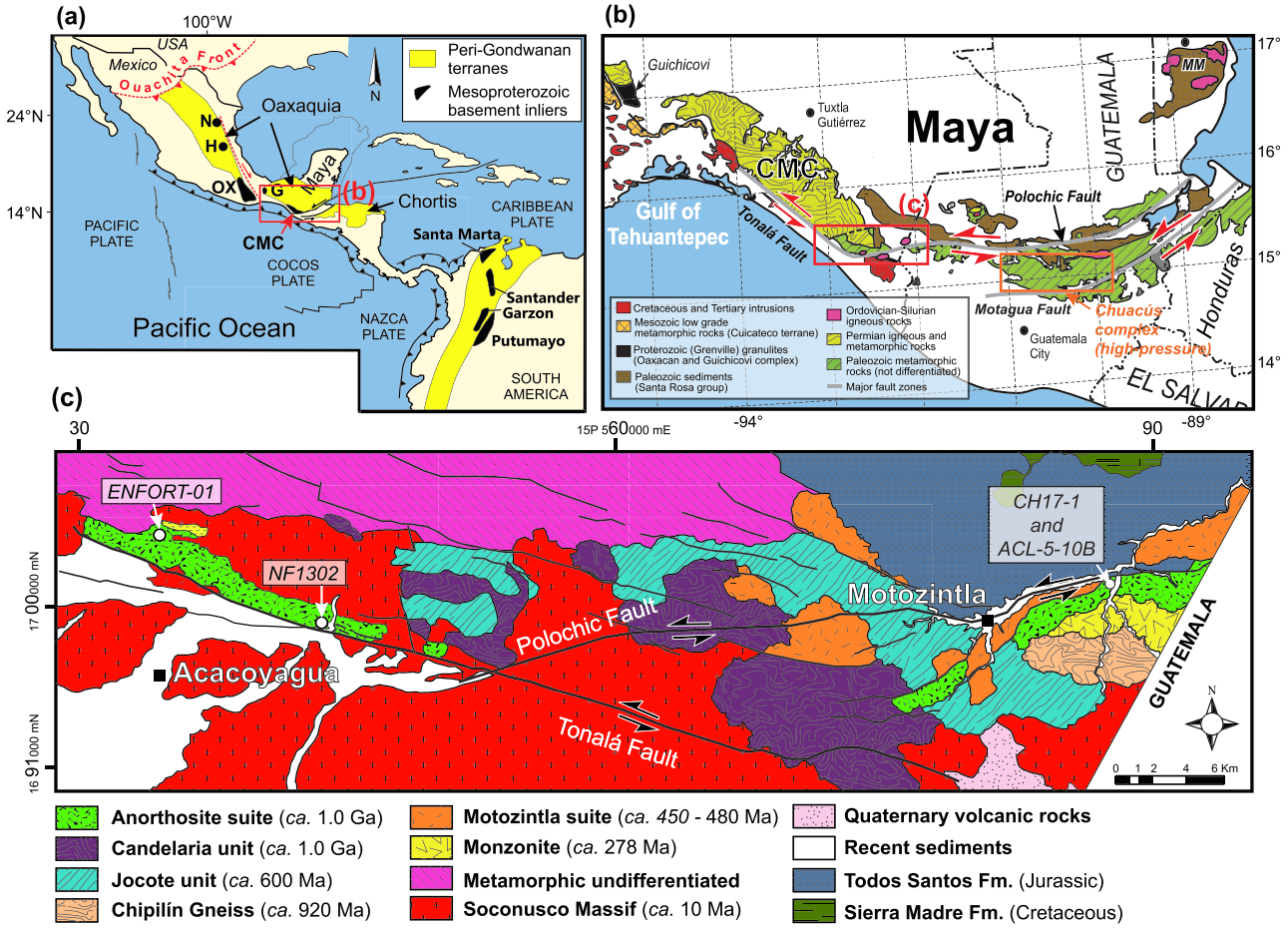

FIGURE 1 Geological setting of the studied area. (a) Plate tectonic overview of Central America showing peri-Gondwanan terranes with Mesoproterozoic basement inliers including Oaxaquia, Maya and Chortis Block as well as the northern Andes (modified after Weber et al., 2018). (b) Geologic map showing pre-Mesozoic rocks exposed in southern Mexico and Central America (modified after French & Schenk, 2006; Martens et al., 2012; Ortega-Gutiérrez et al., 1992, 2007). (c) Geologic map of the study area with sample locations (modified after Cisneros de León et al., 2017). Abbreviations: CMC, Chiapas Massif Complex; G, Guichicovi Complex; H, Huiznopala Gneiss; MM, Maya Mountains; N, Novillo Gneiss; OX, Oaxacan Complex.

Hidalgo, Huitzo, Guichicovi, Huiznopala, and Novillo; Lawlor et al., 1999; Paulson, 1964; Weber et al., 2018, 2010; Weber & Hecht, 2003; Figure 1a). The anorthosite suite in the CMC comprises a set of elongated bodies exposed along the western terminus of the North American and Caribbean plate boundary (Polochic-Motagua fault system active since c. 12 Ma; Figure 1b; Authemayou et al., 2011; Guzmán-Speziale & Meneses-Rocha, 2000). Anorthosites north of the Polochic fault are named Soconusco, whereas those displaced ~70 km to the east and south of the fault are known as Mariscal (Cisneros de León et al., 2017; Figure 1c). Anorthosite occurs spatially associated with banded and folded amphibolitic-granitic gneisses with protolith ages of c. 1.01 Ga and Tonian metamorphic overprint at c. 940–960 Ma (Candelaria Unit; Valencia-Morales et al., 2022; Weber et al., 2018) and also with amphibolitic-granitic gneisses of unknown protolith age but well-defined metamorphic overprint at c. 920 Ma (Chipilín Gneiss; Cisneros de León et al., 2017; Weber et al., 2018, 2020). Ediacaran meta-sediments with oceanic affinity structurally overlie the anorthosite and coeval units (Jocote Unit; González-Guzmán et al., 2016). Both meta-sedimentary and meta-igneous units are intruded by mafic dyke swarms with E-MORB affinity (Cisneros de León et al., 2017; González-Guzmán et al., 2016; Weber et al., 2018, 2020). Zircon crystals from anorthosite in contact with mafic dykes recrystallized during contact metamorphism, indicating dyke intrusion at c. 620 Ma (Cisneros de León et al., 2017; Weber et al., 2020).

The southeastern CMC experienced protracted I-type and muscovite- and garnet-bearing granitic intrusions from c. 480 to 450 Ma (Estrada-Carmona et al., 2012) followed by amphibolite facies metamorphism at c. 450 Ma (~650°C/~6 kbar; González-Guzmán et al., 2016; Weber et al., 2018) that is interpreted as an extension of the Famatinian orogen associated with the closure of the Iapetus Ocean (Weber et al., 2018). After the final amalgamation of Pangea during the Late Permian, granitoid plutons intruded the CMC from c. 280 to 250 Ma and comprise today the bulk of the CMC (Coombs et al., 2020; Schaaf et al., 2002). Plutonic intrusions were shortly followed by regional metamorphism at c. 250 Ma; however, this event is still poorly constrained and may have reached significantly different P–T conditions throughout the CMC as suggested by the preservation of Ordovician Ar ages in hornblende (Estrada-Carmona et al., 2012), while extensive anatexis occurred in other areas (i.e., La Sepultura unit; Weber et al., 2007). Late Miocene granitic arc plutons (Soconusco Massif; *c.* 10 Ma; Molina-Garza et al., 2015) intruded syn-tectonically the southwestern limit of the CMC (especially into anorthosites exposed in the west), and their emplacement was controlled by a crustal-scale shear zone known as the Tonalá shear zone. Mylonitization along this shear zone affected both plutons and basement rocks erasing most of the metamorphic textural context of rocks outcropping nearby (e.g., anorthosites and oxide-apatite-rich amphibolite).

3 | METHODS

3.1 | Samples and sample preparation

For this work, we studied one Mariscal anorthosite sample (CH17-1; zircon U–Pb dating) and RBI deposit from the area near Motozintla (ACL-5-10B; mineral compositions; zircon U–Pb dating, trace elements, oxygen isotopes, and thermometry; rutile U–Pb dating and thermometry). Additionally, one anorthosite sample from the western Soconusco exposure near Acacoyagua (ENFORT-01; rutile U–Pb dating) and a spatially related oxide-apatite-rich amphibolite (OARA) sample (NF1302; zircon U–Pb dating) were also studied.

Given the low abundance of zircon in the anorthosite (CH17-1) and OARA (NF1302) samples as well as extremely low-U content in zircon from the RBI sample (ACL-5-10B), zircon crystals from these samples were separated from the host rock to be analysed by an *ex situ* approach. By contrast, the minute size of baddeleyite grains precluded its effective separation from the host rock, and thus, *in situ* analysis was preferred for this phase as well as for zircon grains in the OARA sample (NF1302). Coarse rutile grains were also analysed *in situ* to avoid mixing with other rutile generations. Anorthosite and OARA samples were initially crushed and sieved, and zircon grains were subsequently separated using a Wilfley shaking table. The RBI sample was crushed, sieved and directly passed through a Frantz magnetic separator to separate zircon and rutile from the ilmenite matrix. All zircon grains were hand-picked under a binocular microscope. Once separated, zircon crystals were mounted together with zircon references AS3 (Booth et al., 2005; Schmitz et al., 2003) and 91500 (Wiedenbeck et al., 2004) and cast into epoxy resin. Epoxy mounts were ground with silicon carbide abrasives until the mid-planes of the zircons were exposed and then polished using diamond abrasive (1 μm). Before analysis, polished zircons were imaged by backscattered electron (BSE) and cathodoluminescence (CL) methods, to reveal intragrain growth domains, inclusions and potential radiation-damaged zones. All *in situ* targeted minerals (zircon, baddeleyite and rutile) from RBI (ACL-5-10B) and OARA (NF1302; only zircon) were initially located in petrographic thin sections by combining BSE imaging, energy dispersive X-ray analysis and CL. To enhance

the localization of zircon and baddeleyite and to avoid confusion with small magnetite crystals in BSE images (appearing at a similar grayscale), we exploited the luminescent nature of zircon and baddeleyite by using CL detection. This unambiguously identified zircon and baddeleyite crystals in the rock. Subsequently, regions of interest were cut out from the thin sections using a low-speed diamond saw and mounted in epoxy together with previously polished epoxy blocks that contained Phalaborwa baddeleyite (2059.8 ± 0.8 Ma; Heaman & LeCheminant, 1993), AS3 zircon (1099.1 ± 0.5 Ma; Schmitz et al., 2003), 91500 zircon (Wiedenbeck et al., 2004) and R10b rutile reference crystals (1090 ± 5 Ma; Luvizotto et al., 2009).

3.2 | Mineral compositions

Mineral analyses were carried out on thin sections at the Institute of Earth Sciences at Heidelberg University, Germany, with a CAMECA SX51 EMP equipped with five wavelength-dispersive spectrometers (WDS). Standard operating conditions were 15 kV accelerating voltage, 20 nA beam current and a beam diameter of ~1 μm. Natural and synthetic oxide and silicate standards were used for calibration. Matrix corrections were done online with the "PAP" algorithm (Pouchou & Pichoir, 1985). EMP line profiles were measured across six thin section domains from the RBI sample (ACL-5-10B) that included coarse-grained rutile, zircon coronas, ilmenite and högbomite as well as one profile across spinel partly replaced by högbomite. Altogether, 1100 individual points were analysed.

3.3 | Trace elements in zircon

Trace element abundances in zircon separates from the RBI sample (ACL-5-10B) were analysed using a CAMECA IMS 1280-HR secondary ion mass spectrometer (SIMS) at the Institute of Earth Sciences, Heidelberg University, Germany. The trace element routine included the complete suite of rare earth elements (REE) plus $^{49}Ti^{+}$, $^{177}Hf^{++}$, $^{89}Y^{+}$, $^{178}Hf^{+}$, $^{232}Th^{+}$ and $^{238}U^{+}$; besides, $^{26}Mg^{+}$, $^{31}P^{+}$ and $^{57}Fe^{+}$ were also detected as monitors for beam overlap onto inclusions, and $^{30}Si^{+}$ was used as a normalizing species. Secondary ions were generated by $^{16}O^{-}$ primary ion beam impact at a current of 15–20 nA within an oval spot ~35 μm in maximum diameter. Secondary ions were then extracted by applying a voltage of +9.9 kV for the mass spectrometer tuned for transmission of 10 keV secondary ions and an energy bandpass of 50 eV. A moderate mass resolving power of ~1000 was applied, reducing contributions for most molecular interferences, which were nonetheless monitored on interference-free doped glasses leading to minor corrections of light REE (LREE) oxides interfering with heavy REE (HREE); similarly, the contributions of hydrides (e.g., ^{140}CeH on ^{141}Pr) and doubly charged ions ($^{178}Hf^{++}$ on ^{89}Y) were corrected. All interference-corrected trace element intensities were normalized to $^{30}Si^{+}$, to mitigate the effects of primary current instability or time-dependent variations in secondary ion yields. The relative sensitivity factor (RSF) values were calibrated by measurements of the NIST 610 glass standard under the same conditions as zircon analyses. Zircon reference 91500 was also analysed to monitor bias due to matrix effects; critical trace elements (e.g., Ti, Y and Hf) closely agree with reported values (Szymanowski et al., 2018; Wiedenbeck et al., 2004). Furthermore, all analyses with elevated counts for Mg, P and Fe relative to zircon reference 91500 were excluded from further consideration due to suspected beam overlap onto glass or mineral inclusions.

3.4 | Oxygen isotopes in zircon

Oxygen isotopes in zircon separates from the RBI sample (ACL-5-10B) were also analysed employing SIMS at the Institute of Earth Sciences, Heidelberg University. Analyses were performed using Faraday cup (FC) multicollection mode and a Cs^{+} primary beam with an intensity of ~2 nA focused into an ~8–10 μm diameter spot. An electron gun with a normal incidence at equal potential to the sample surface provided self-regulating charge compensation. Negative secondary ions were extracted with a −10 kV acceleration voltage. Bracketing and interspersed analyses of zircon reference AS3 ($\delta^{18}O_{VSMOW} = +5.344‰$; Trail et al., 2007) and 91500 ($\delta^{18}O_{VSMOW} = +9.86‰$; Wiedenbeck et al., 2004) were executed to track instrumental mass fractionation (IMF) and correct isotopic ratios of the unknowns. FC backgrounds were recorded before each spot analysis to monitor drift but averaged over the entire session as no drift was detected. Uncertainties are based on the external reproducibility of the zircon reference and reported in all cases at one standard deviation (1 s.d.). The standard deviation for interspersed AS3 and 91500 zircon reference analyses over the entire duration of analyses is 0.28‰ and 0.13‰, respectively.

3.5 | Ti-in-zircon and Zr-in-rutile thermometry

Titanium-in-zircon temperature estimates were calculated using the equation from Ferry and Watson (2007).

A fixed value for $aTiO_2$ and $aSiO_2$ of 1 was applied based on the ubiquitous presence of rutile and the interstitial presence of quartz in the sample. Zirconium concentrations of selected rutile grains from the RBI sample (ACL-5-10B) were determined by EMP at Heidelberg University. Analytical conditions were optimized specifically for Zr and include simultaneous measurement of the Zr Lα peak on four different detectors with 100 × 10 s counting times using a 200 nA beam current, an acceleration voltage of 20 kV and a beam size of 5 μm. A fifth spectrometer was tuned to the Si Kα peak to monitor variations associated with inclusions or secondary fluorescence. Calibration was done on four different rutile references, each with a different Zr concentration, including a synthetic grain with no Zr and the natural R10 (789 ppm Zr), R19 (264 ppm Zr) and Diss (98 ppm Zr) rutile reference material, which have been extensively examined by Zack, Moraes, et al. (2004) and Luvizotto et al. (2009). Average Zr concentration from rutile R10 was 792 ± 7 ppm (n = 9) and for R19 was 258 ± 19 ppm (n = 9). For temperature calculations, equation 14 from Ferry and Watson (2007) was employed and compared with other thermometers (Table S4), overall yielding similar results (e.g., Tomkins et al., 2007). Given the dependency of Zr-in-rutile concentrations on the $aSiO_2$ in the system, we employed an $aSiO_2$ value of 1 given the presence of scarce interstitial quartz grains. The precision of the Zr-in-rutile thermometer is <3% for Zr concentrations above 100 ppm, and between 4 and 8% for <100 ppm Zr. Uncertainties were calculated considering end-member scenarios for the given analytical uncertainty of Zr analysis and the inherent uncertainties from the Ferry and Watson (2007) Zr-in-rutile calibration.

3.6 | Multiphase SIMS dating (U–Pb)

3.6.1 | Zircon and baddeleyite dating

For zircon separates and *in situ* zircon and baddeleyite dating, similar SIMS analytical conditions were applied. A mass-filtered $^{16}O^-$ beam was focused to an ~10 to 25 μm diameter spot, and secondary ions were extracted at 10 kV. Oxygen flooding was used to enhance Pb^+ yields (~7× for baddeleyite) and mitigate crystal orientation bias in U–Pb relative sensitivity. To avoid secondary ions from the periphery of the analysis crater (neighbouring minerals), the field aperture was narrowed to an ~10 × 10 μm^2 effective sampling area. Depending on the availability of material during individual analyses, between 8 and 24 cycles were accumulated. Isotope ratios were corrected for common Pb using either measured common ^{208}Pb (after correction of *in situ* production of ^{208}Pb from ^{232}Th) or ^{204}Pb. Low-radiogenic zircon was plotted uncorrected for common-Pb, and lower intercept model ages were determined. Analysis of reference zircon 91500 with a known composition (~82 ppm U; Wiedenbeck et al., 2004) was used to estimate the U content of zircon targets. A weighted mean age for zircon reference AS3 yielded a $^{207}Pb/^{206}Pb$ age of 1096 ± 3 Ma (2σ; n = 28) and MSWD of 0.88, whereas the Phalaborwa baddeleyite reference yielded a $^{207}Pb/^{206}Pb$ age of 2059 ± 4 Ma (2σ; n = 21). Given the relatively low content of U in most of the analysed zircon crystals, the $^{206}Pb/^{238}U$ dates were preferentially used for interpretation of zircon <800 Ma and $^{207}Pb/^{206}Pb$ dates for zircon >800 Ma; all individual zircon age uncertainties hereafter are reported as 1σ. Zircon dates include full propagation of systematic and random uncertainties.

3.6.2 | *In situ* rutile dating

In situ rutile U–Pb dating for the RBI (ACL-5-10B) and anorthosite (ENFORT-01) samples was performed following instrumental conditions described in Schmitt and Zack (2012). Rutile reference R10b, normalized to its average age, yielded a weighted mean $^{206}Pb/^{238}U$ age of 1090 ± 14 Ma (2σ; n = 12; MSDW = 0.55), which is used here as a measure of analytical reproducibility.

4 | RESULTS

4.1 | Mineralogy

Detailed field descriptions of anorthosite and related rocks can be found in Cisneros de León et al. (2017). Based on new observations, we present an updated overview of the mineralogy and textural characteristics of anorthosites and Ti-Fe-oxide-rich rocks initially described by Cisneros de León et al. (2017).

4.1.1 | Anorthosite (CH17-1)

The anorthosite is composed of >95% recrystallized andesine plagioclase with accessory rutile, ilmenite, amphibole, quartz (interstitial), apatite, zircon and rare garnet (Figure 2a,b). Amphibole is the most common mafic mineral observed and generally occurs in a low proportion (<3%). Secondary minerals commonly present are muscovite, titanite and epidote. Rutile occurs as relicts partly transformed into titanite or as rims around ilmenite (Figure 2c–e). Ilmenite crystals are usually surrounded by a corona of biotite (Figure 2b).

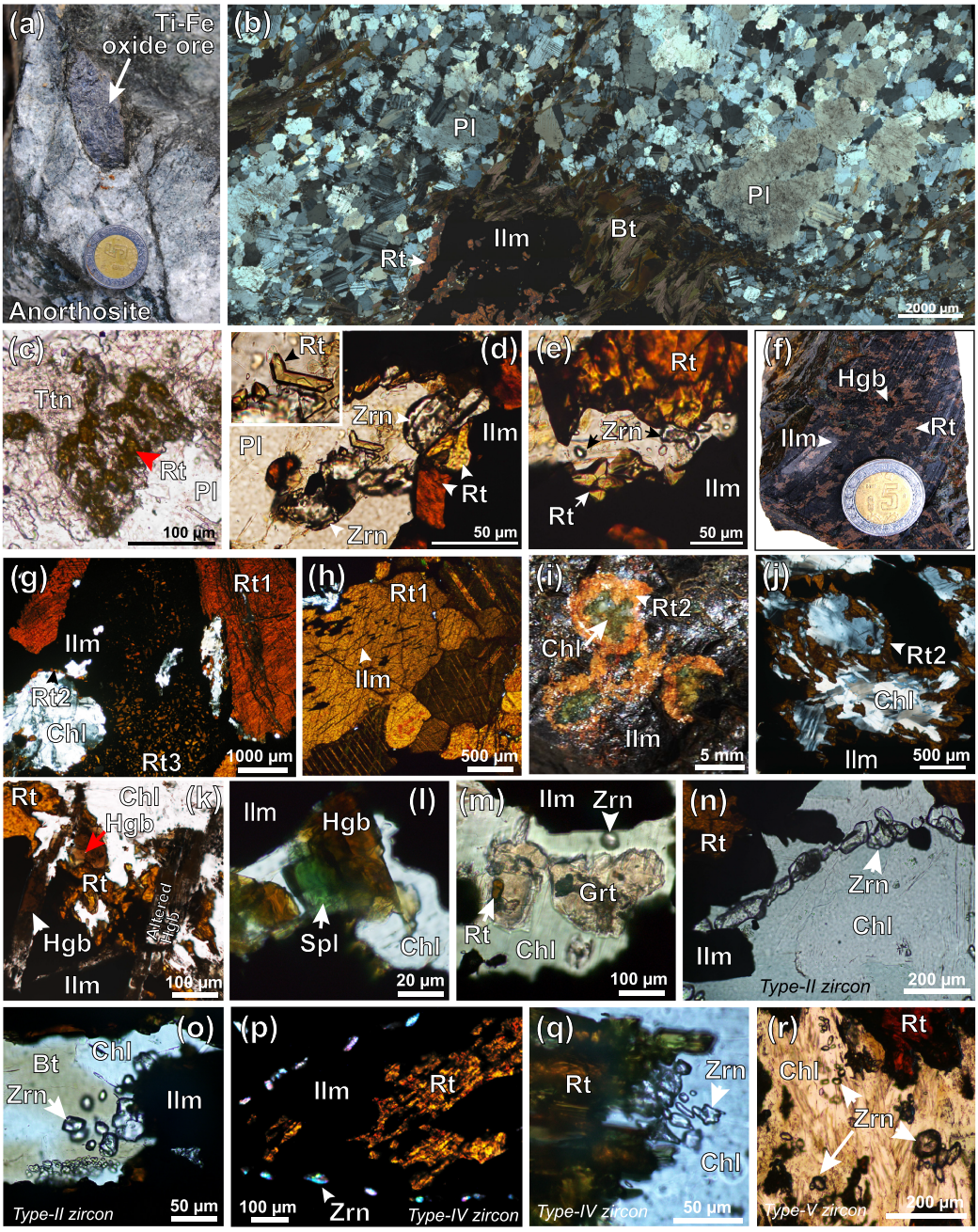

FIGURE 2 Hand sample photos and photomicrographs of anorthosite and rutile-bearing ilmenitite. (a) Rutile-bearing ilmenitite included in anorthosite at hand sample scale. (b) Anorthosite in thin section showing a recrystallized plagioclase matrix containing ilmenite grains rimmed by rutile and biotite. (c) Rutile relicts within titanite in the anorthosite matrix. (d,e) Rutile rims around ilmenite grains in anorthosite showing development of metamorphic zircon. (f) Rutile-bearing ilmenitite hand sample showing coarse-grained rutile, ilmenite, and högbomite grains. (g) Different textures of rutile (Rt) co-existing in the rutile-bearing ilmenitite; Rt1 is coarse-grained rutile of up to 1 cm in diameter; Rt2 occurs at the boundaries between chlorite lenses and ilmenite; Rt3 shows a symplectitic texture with haematite hosted in ilmenite grains. (h) Typical ilmenite exsolution needles and polysynthetic twinning in coarse-grained rutile. Large rutile grains are typically recrystallized into smaller grain sizes and show 120° joints. (i) Rutile-bearing ilmenitite hand sample showing large and round chlorite lenses rimmed by rutile. (j) Round chlorite lenses with rutile rims in thin section. (K) Prismatic högbomite partly altered into chlorite. Rutile and zircon occur often around altered prismatic högbomite. (l) Högbomite replacing spinel (pleonaste) within a chlorite lens (m) garnet partly altered to chlorite preserving a rutile inclusion. Rounded zircon crystals occur next to garnet. (n,o) Zircon at the grain boundaries or former grain boundaries of ilmenite in contact with chlorite. (p) Coarse-grained rutile partly transformed into ilmenite showing discontinuous zircon coronas at the former rutile grain boundary. (q) Zircon forming after the breakdown of rutile within a chlorite lens. (r) Zircon accumulation within a chlorite and biotite lens. The coin diameter is 2.5 cm. Mineral abbreviations after Whitney and Evans (2010).

Zircon occurs frequently at the borders of ilmenite and/or rutile grains (Figure 2d,e).

4.1.2 | Rutile-bearing ilmenitite (ACL-5-10B)

The rutile-bearing ilmenitite is essentially composed of ilmenite and rutile occurring in a granoblastic coarse-grained texture (Figure 2f). Minor phases include Ti-magnetite, haematite, baddeleyite (ZrO_2), srilankite ($ZrTi_2O_6$), spinel (pleonaste), zircon, högbomite ($[Mg,Fe^{2+}]_2[Al,Ti]_5O_{10}$), zirconolite ($CaZrTi_2O_7$), chlorite, plagioclase, epidote and rare quartz and garnet. Ilmenite is the dominant mineral (60–90%), commonly showing fine haematite exsolution lamellae. Rutile is the second-most abundant mineral (10–40%) and occurs at least in three different textural settings (Figure 2g–j): (1) coarse-grained rutile (0.1–10 mm) in equilibrium with the ilmenite matrix; ilmenite exsolution needles and polysynthetic twinning are characteristic of this morphology (Figure 2h); (2) rutile rims around chlorite lenses (Figure 2i,j) and (3) symplectitic intergrowth of rutile and haematite hosted in ilmenite (Figures 2g and 3c). Högbomite occurs in two different textural

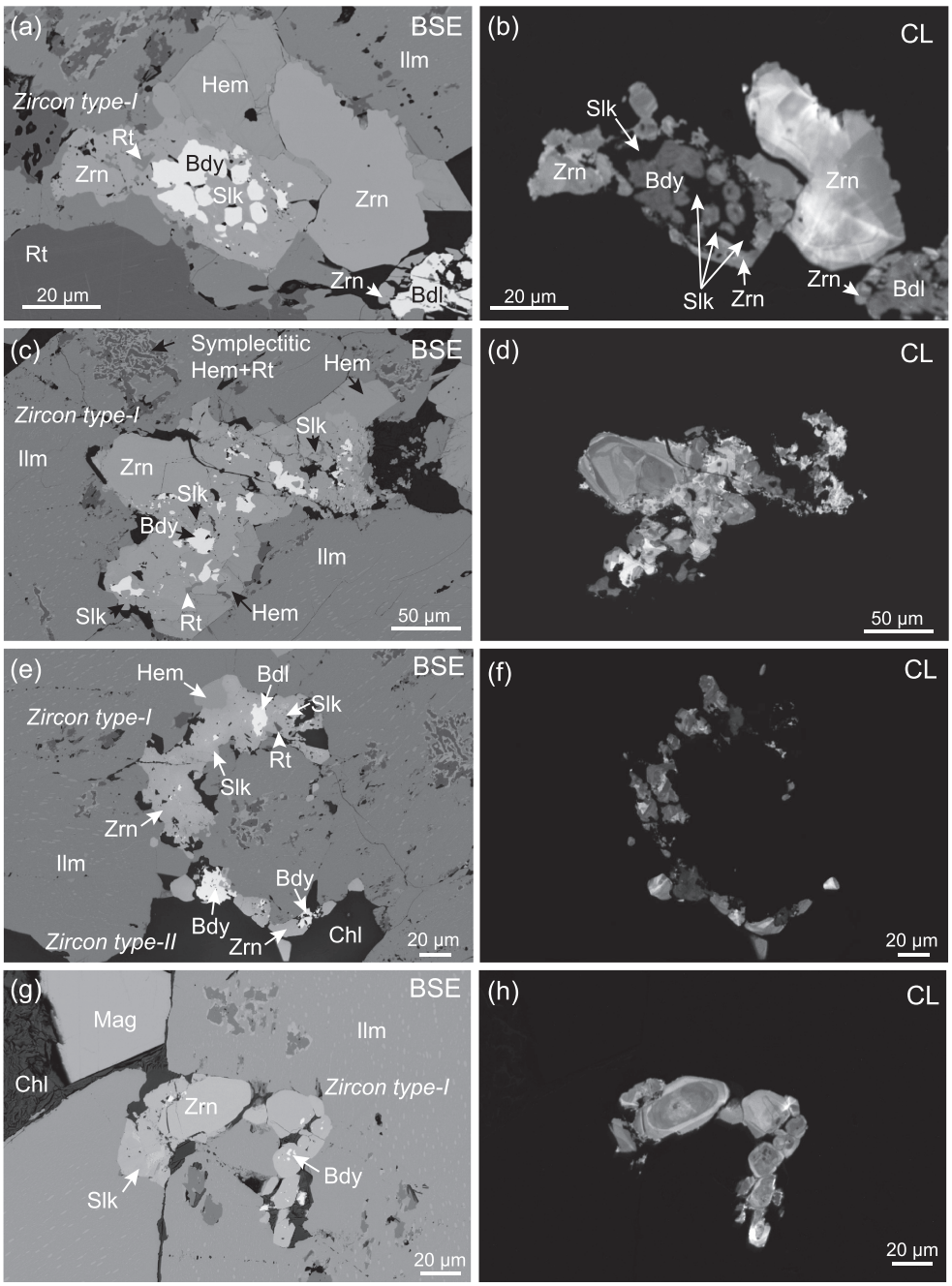

FIGURE 3 Backscattered electron (BSE) images from rutile-bearing ilmenitite (ACL-5-10B) showing textures of zircon formed at ilmenite interstices (*type-I*) and next to chlorite lenses (*type-II*) as well as corresponding cathodoluminescence (CL) images. (a–h) Textures preserving baddeleyite reaction into srilankite (Slk) and srilankite into zircon. Haematite occurs often filling voids. Panel (e) shows the spatially close co-existence of *type-I* zircon with *type-II* zircon formed along ilmenite grain boundaries and in contact with chlorite lenses. Srilankite is rarely observed associated with *type-II* zircon. Panels (a) and (b) are modified from Cisneros de León et al. (2017).

settings: (1) as large prismatic crystals partly replaced by chlorite (up to 1 cm; Figures 2k and 4a–d) and (2) as the outcome of spinel breakdown (Figure 2l). The breakdown of prismatic högbomite into chlorite is usually accompanied by the formation of rutile at its borders (Figures 2k and 4e). In both textures, högbomite is replaced by chlorite and minor haematite blebs (Figures 2k and 4a–d), and in some cases, högbomite is almost completely replaced by haematite (Figure 4f). Relict garnet with rutile inclusions was observed partly replaced by chlorite; rounded zircon crystals were found within the chlorite and next to relict garnet (Figure 2m).

Zircon crystals around Ti-Fe oxide minerals are abundant and can be classified in at least five different textural types (identified by Roman numerals I–V). *Type-I* zircon is usually found interstitial to ilmenite grains and texturally occurs as overgrowths over srilankite crystals which previously formed at the expense of baddeleyite (Figure 3a–h). Baddeleyite relicts are well-preserved in most cases, and the textural relationship among baddeleyite, srilankite and zircon is easily revealed by CL imaging, where srilankite displays no CL emission, and baddeleyite shows lower intensity than zircon (Figure 3b). *Type-II* zircon occurs along grain boundaries of ilmenite and in contact with chlorite lenses (Figures 2n–o and 5a–d). *Type-II* zircon exhibits coarser grain sizes relative to *type-I* zircon. Frequently, subprismatic habits and baddeleyite relicts are observed (Figure 5a–d). Only in rare cases, srilankite is associated with this texture. T*ype-III* zircon occurs at the borders or within prismatic högbomite crystals; it also occurs commonly associated with srilankite and baddeleyite relicts (Figure 4a–d). *Type-IV* zircon is found outlining coarse-grained rutile crystals (Figures 2p–q and 6) and preserved baddeleyite relicts. In some cases, *type-IV* zircon coronas outline former rutile borders now replaced by ilmenite or in rare cases around rutile within chlorite lenses (Figure 2q). Rutile associated with zircon coronas without retrogression to ilmenite commonly exhibits translucent, amber-coloured zones next to neoformed zircon (Figure 2q). The morphology of *type-IV* zircon ranges from round to ovoid and sizes from 30 to 120 μm. *Type-V* zircon is present as randomly distributed accumulations

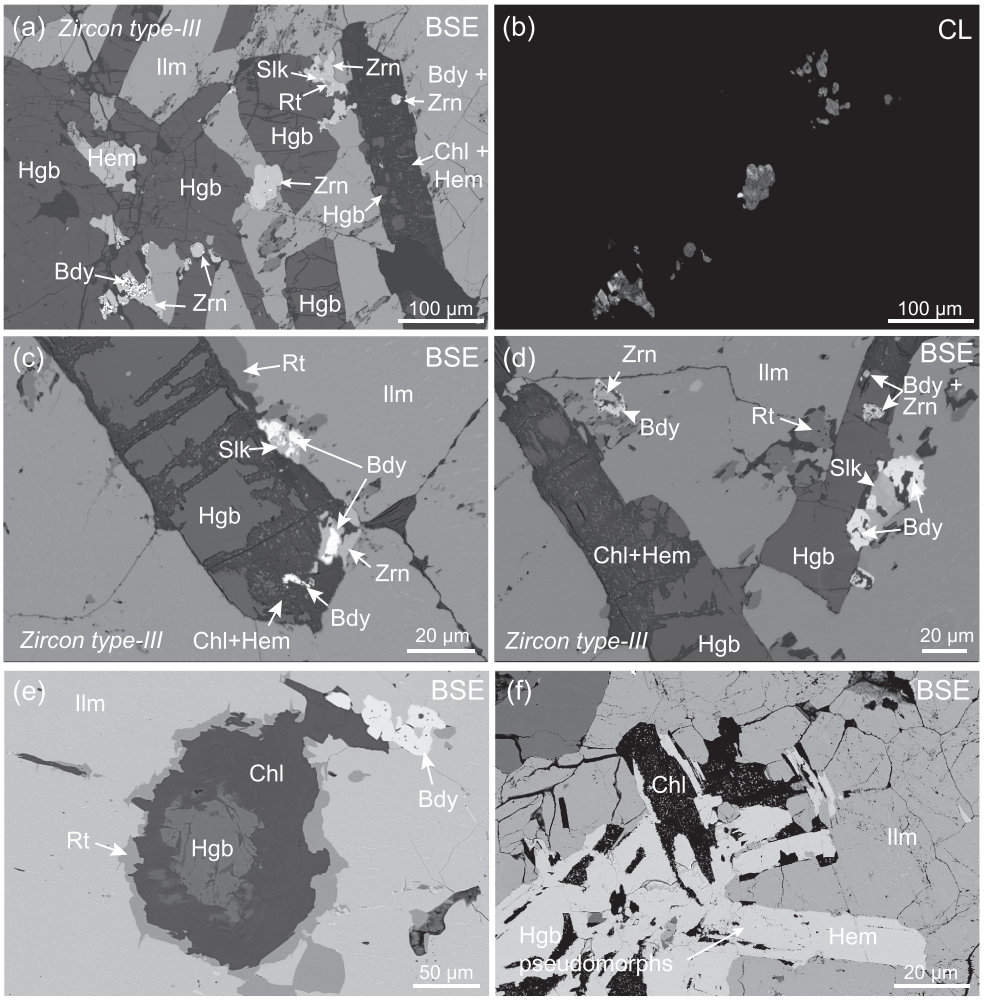

FIGURE 4 Backscattered electron (BSE) images from rutile-bearing ilmenitite (ACL-5-10B) displaying textures of högbomite and corresponding cathodoluminescence (CL) image of associated zircon (*type-III*) and baddeleyite. (a–d) Prismatic högbomite partially replaced by chlorite and minor haematite (small brighter dots), showing at its borders small grains of baddeleyite rimmed by srilankite or zircon. (e) Högbomite crystal replaced by chlorite and showing rutile growth at the interface between ilmenite and chlorite. (f) Haematite pseudomorphs after prismatic högbomite. Panel (d) is modified from Cisneros de León et al. (2017).

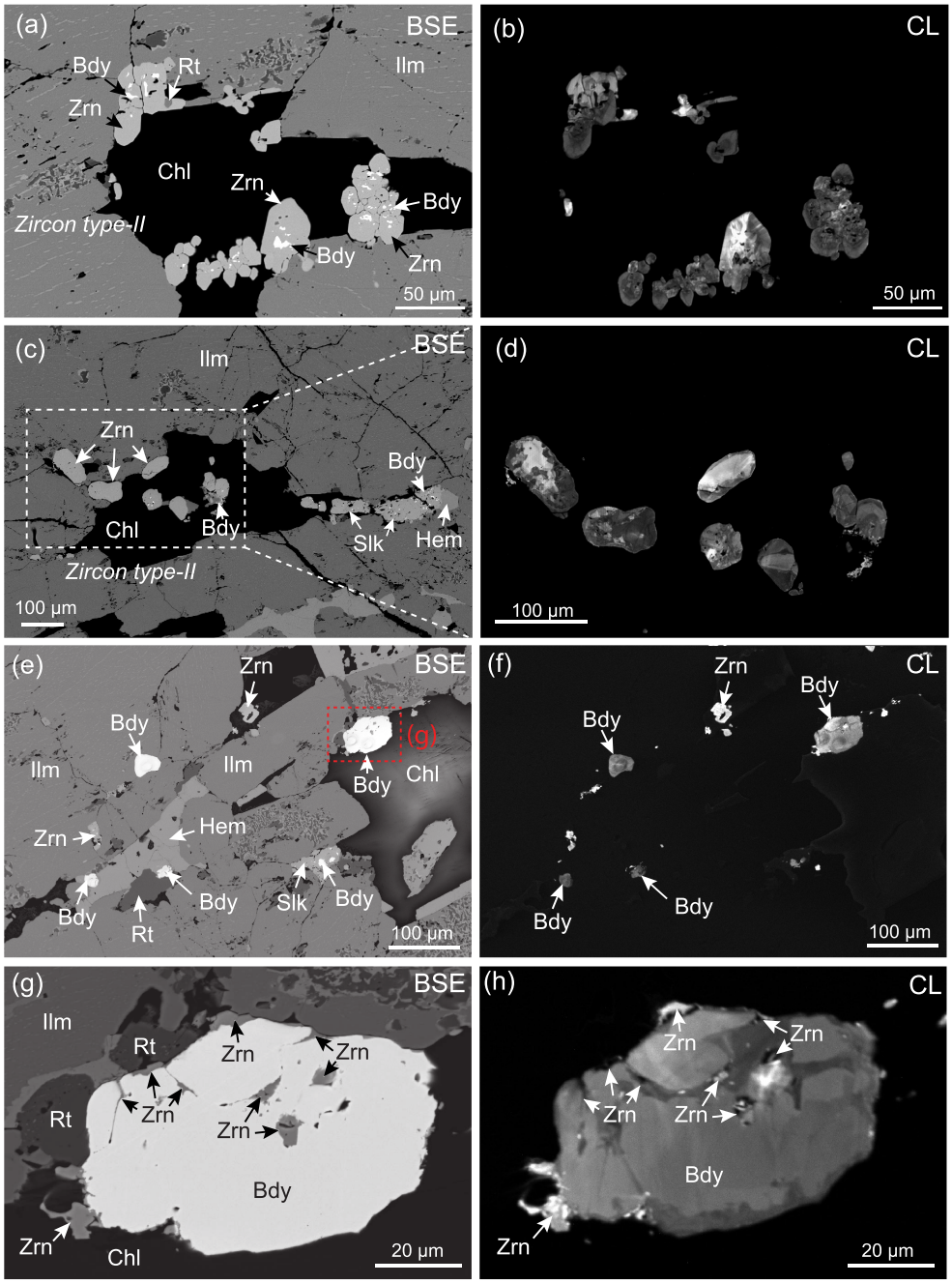

FIGURE 5 Backscattered electron (BSE) images from rutile-bearing ilmenitite (ACL-5-10B) illustrating textures of zircon (*type-II*) and baddeleyite formed at ilmenite grain boundaries and corresponding cathodoluminescence (CL) images. (a–d) Zircon grains along ilmenite boundaries showing baddeleyite relicts and in some cases rutile inclusions. (e–f) Baddeleyite with incipient or no zircon formation at its borders. (g) Baddeleyite crystal at the border of an ilmenite grain and next to chlorite; baddeleyite shows incipient transformation into zircon along fractures or cavities. (h) CL from baddeleyite crystal in (g) showing mostly homogeneous CL domains with darker CL zones where zircon transformation occurred. Panel (a) is modified from Cisneros de León et al. (2017).

within chlorite and biotite lenses away from ilmenite grain boundaries (Figure 2r), displaying a wide range of sizes (5–150 µm) and shapes (equant, prismatic and anhedral).

Although most baddeleyite crystals are spatially associated with zircon and srilankite, there are cases where baddeleyite is found as pristine grains or showing only incipient transformation to other Zr-rich phases (i.e., zircon, srilankite and zirconolite; Figure 5e–h). These baddeleyite crystals were usually found interstitially between ilmenite grains, although some exceptions were observed where large baddeleyite crystals (~100 µm) are in contact with chlorite (Figure 5e–f).

4.1.3 | Oxide-apatite-rich amphibolite (OARA; NF1302)

Oxide-apatite-rich amphibolite has been only observed near the village of Nueva Francia near Acacoyagua (Figure 1) within a highly deformed zone associated with the Tonalá shear zone. Its exposure is subordinate when compared with RBI and hornblendite. OARA rocks are strongly overprinted by penetrative ductile deformation that erased possible crosscutting relationships with anorthosite. Nonetheless, deformed anorthosite enclaves of variable sizes (from millimetres to metres) occur frequently within OARA and nelsonite

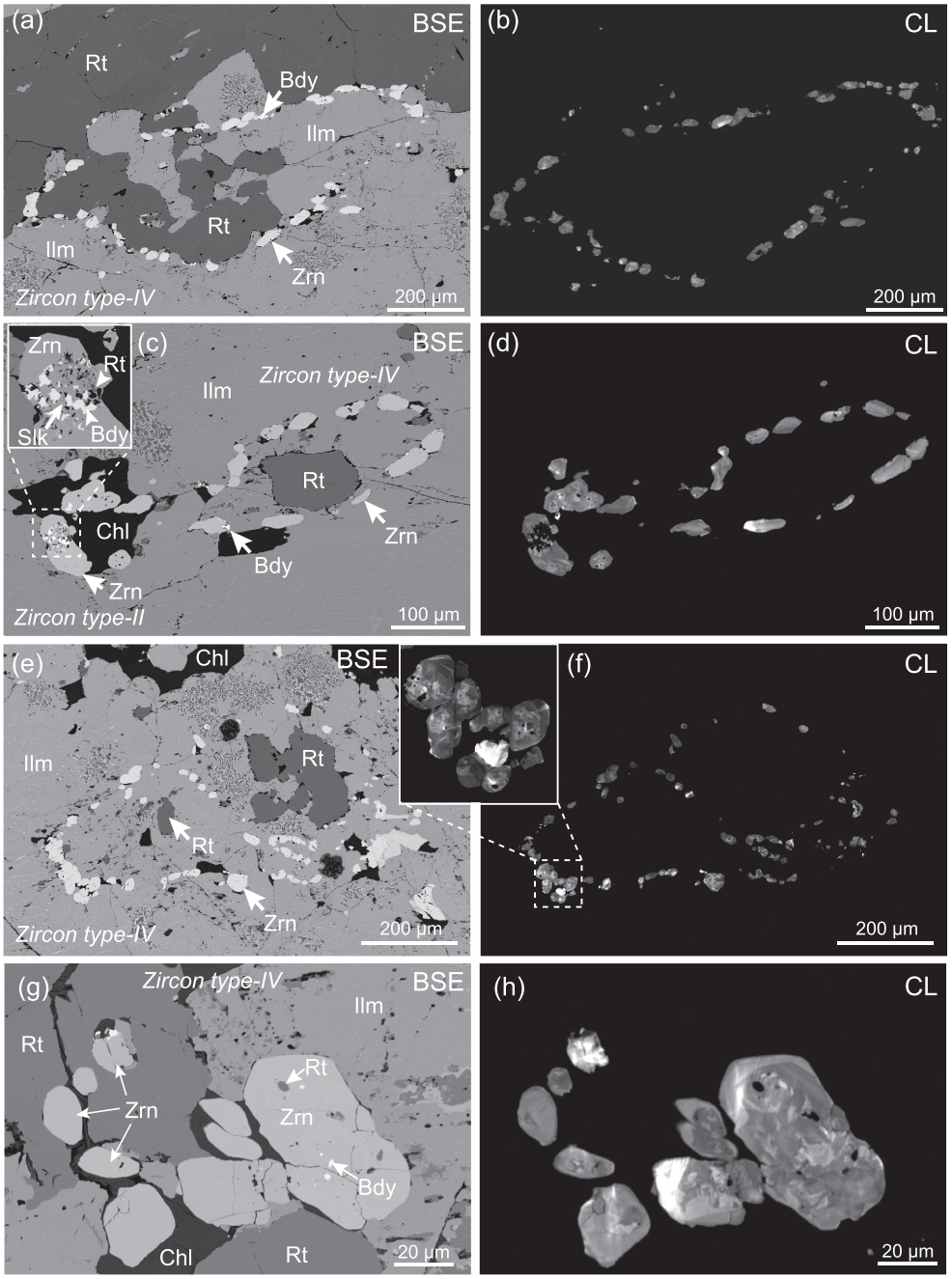

FIGURE 6 Backscattered electron (BSE) images from rutile-bearing ilmenitite (ACL-5-10B) showing textures of discontinuous *type-IV* zircon coronas around coarse-grained rutile and corresponding cathodoluminescence (CL) images. (a–f) Rutile partially retrogressed to ilmenite showing discontinuous zircon coronas delimiting the initial rutile grain boundary. Zircon crystals contain small baddeleyite relicts. (g,h) Zircon crystals spatially associated with rutile showing no apparent retrogression to ilmenite. Note that zircon also occurs inside the rutile grain and preserves baddeleyite relicts.

(Cisneros de León et al., 2017). OARA contains mainly hornblende (50%), subordinate ilmenite (15%), magnetite (5%), plagioclase (20%) and apatite (10%). Mineral foliation and stretching of ilmenite (large ribbons) reflect pervasive ductile deformation. Rutile and biotite are observed as rims around elongated ilmenite grains. Secondary zircon along ilmenite borders is also a common feature in this rock. These zircon crystals are ovoid to round in shape and their size varies from ~20 to 150 µm (Figure 7a–d). However, they are commonly deformed and broken. A few zircon grains occur within anorthosite micro-enclaves (0.5–1 cm), showing semi-prismatic morphologies (Figure 7e–f).

4.2 | Mineral compositions

Major-element chemical analyses were performed on some accessory and major rock-forming minerals from the RBI (ACL-5-10B; Table 1 and Dataset S1). For most of the analysed elements in högbomite, chemical differences between prismatic grains and that replacing spinel are subtle, but significant differences exist in MgO and Al_2O_3 (Figure S1): prismatic högbomite is enriched in Al_2O_3 and MgO relative to högbomite that replaces spinel. Chemical variations between spinel and associated högbomite are better depicted in compositional line profiles where disequilibrium textures of högbomite

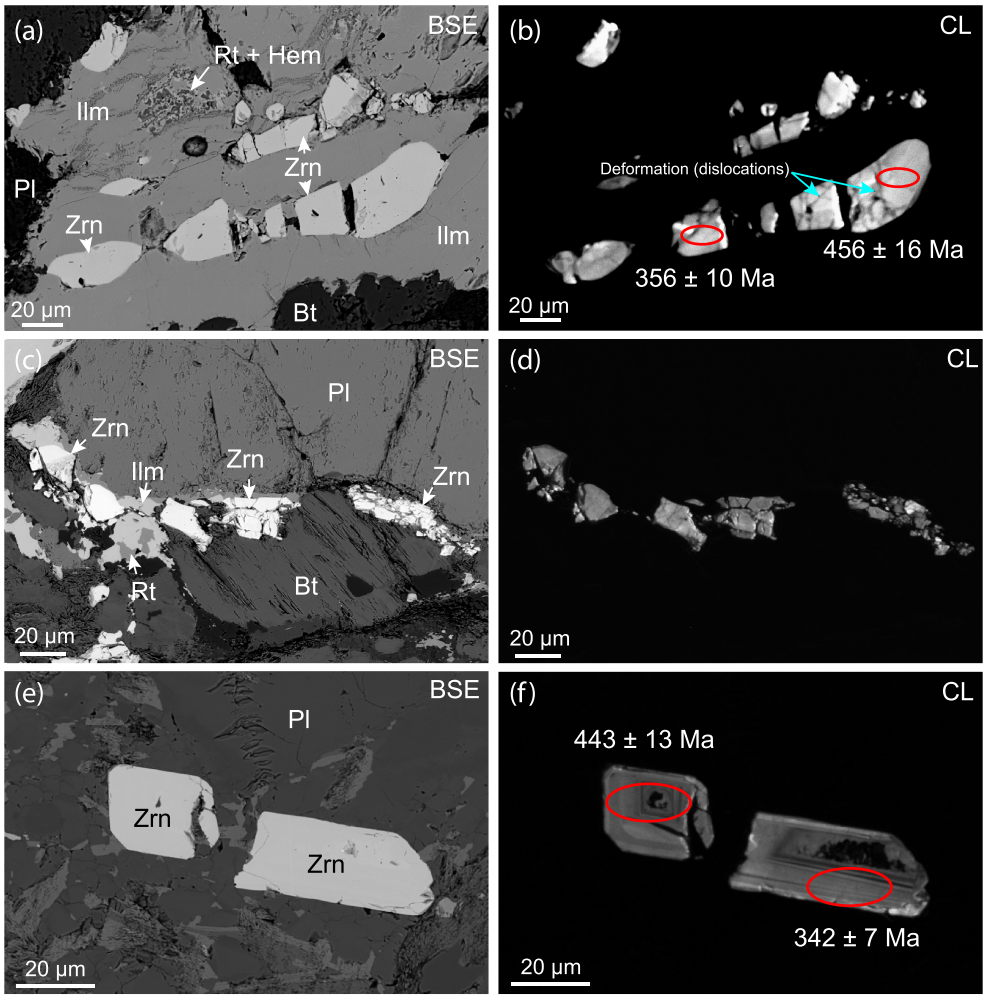

FIGURE 7 Selected backscattered electron (BSE) images of zircon occurring in the oxide-apatite-rich amphibolite (NF1302) and corresponding cathodoluminescence (CL) images. (a–d) Zircon associated with ilmenite showing strong deformation patterns. CL imaging reveals chemically altered domains associated with deformation dislocations (CL darker zones). (e–f) Zircon crystals within the anorthosite micro-enclaves showing seemingly oscillatory CL patterns. Dates on zircon grains are *in situ* SIMS analysis.

replacing spinel are present (Figure S1 and Table S1). Spinel partially replaced by högbomite shows higher concentrations of Cr_2O_3 (~3.45 wt%) and ZnO (~7.66 wt%) relative to högbomite (~1.66 and ~3.40 wt%, respectively), whereas total iron content is similar between both phases (~20 wt%). The Al_2O_3 and MgO contents in högbomite coronas and spinel cores are also similar (Figure S1). By contrast, the TiO_2 compositions exhibit sharp compositional steps at the interface between the spinel (~0.21 wt%) and högbomite (~6.26 wt%; Figure S1). Chlorite average compositions show relatively large standard deviations in SiO_2, Al_2O_3, FeO and MgO (7–11%), suggesting the likely presence of multiple types of chlorite. X-ray diffraction analysis indicates that clinochlore-type chlorite is dominant in the sample (Figure S2), whereas empirical chemical classifications further suggest the presence of sheridianite and corundophilite, which may indicate transformation after distinct ferromagnesian phases. Srilankite appears randomly zoned in backscattered secondary electron images; this variation could be correlated to changes in the elemental proportions of TiO_2, ZrO_2 and total FeO (Table 1). Nevertheless, its composition is similar to srilankite from other occurrences (e.g., Lindås Nappe, Norway; Bingen et al., 2001).

Rutile from all types is the nearly pure TiO_2 endmember (99.2–100 wt%). Except for higher Fe_2O_3 contents in rutile from the symplectitic texture (~1.73 wt%), coarse-grained rutile and rims around chlorite lack any significant compositional variations in Fe_2O_3 and TiO_2 contents. Interestingly, intragrain compositional profiles show internal concave core-to-rim patterns in Zr, Hf and Cr abundances in most coarse-grained rutile (Figure S3); however, the outermost rim domains are depleted in Zr and Hf concentrations, whereas Cr is seemingly uniform (Figure S3).

4.3 | Trace elements in zircon

Zircon separates from the RBI sample range in size from just a few μm up to ≥200 μm in length. Their morphology varies from rounded, anhedral to elongated crystals (Figure 8a). The internal complexity revealed by CL is

TABLE 1 Representative average compositions of rare accessory minerals and major rock-forming minerals in RBI sample (ACL-5-10B)

	Högbomite		Spinel		Chlorite		Srilankite		Ilmenite		Magnetite		Rutile (coarse)		Rutile next to Hög		Rutile rimming Chl		Rutile symplectitic	
Mineral analyses	***n* = 30**	**1 s.d.**	***n* = 6**	**1 s.d.**	***n* = 8**	**1 s.d.**	***n* = 4**	**1 s.d.**	***n* = 9**	**1 s.d.**	***n* = 4**	**1 s.d.**	***n* = 10**	**1 s.d.**	***n* = 3**	**1 s.d.**	***n* = 5**	**1 s.d.**	***n* = 4**	**1 s.d.**
SiO_2 wt%	0.26	0.71	0.17	0.02	25.29	1.77	0.00	0.00	0.01	0.01	0.08	0.12	0.00	0.00	0.09	0.09	0.01	0.01	0.00	0.01
TiO_2	6.14	0.29	0.21	0.02	0.18	0.15	54.52	0.92	50.09	1.37	0.50	0.41	99.84	0.55	99.24	0.23	100.60	0.20	99.17	0.61
ZrO_2	0.03	0.02	0.03	0.02	0.03	0.03	44.78	0.80	0.02	0.02	0.04	0.03	0.12	0.05	0.08	0.04	0.07	0.02	0.00	0.01
Al_2O_3	57.08	1.18	56.59	0.14	27.66	3.11	n.a.	n.a.	0.00	0.00	1.83	2.92	0.00	0.00	0.00	0.00	0.00	0.00	0.00	0.00
Cr_2O_3	1.43	0.37	3.45	0.09	0.21	0.23	0.04	0.02	0.09	0.05	0.71	0.28	0.23	0.04	0.21	0.05	0.20	0.03	0.28	0.16
Fe_2O_3	11.65	0.92	3.30	0.23	0.00	0.00	0.79	0.29	0.00	0.00	65.25	4.81	0.61	0.16	0.71	0.19	0.51	0.10	1.73	0.24
FeO	9.73	1.54	17.57	0.14	8.03	1.55	0.00	0.00	48.30	1.87	31.29	0.37	0.00	0.00	0.00	0.00	0.00	0.00	0.00	0.00
MnO	0.07	0.03	0.11	0.02	0.02	0.01	0.02	0.02	0.35	0.23	0.01	0.01	0.01	0.01	0.00	0.00	0.01	0.01	0.01	0.01
ZnO	3.93	0.65	7.66	0.10	0.06	0.06	0.04	0.04	0.02	0.03	0.26	0.28	0.02	0.03	0.01	0.01	0.03	0.03	0.07	0.05
NiO	n.a.	n.a.	0.00	0.00	0.00	0.00	n.a.	n.a.	n.a.	n.a.	n.a.	n.a.	n.a.	n.a.	n.a.	n.a.	n.a.	n.a.	n.a.	n.a.
MgO	8.79	0.85	10.32	0.06	25.75	0.79	0.01	0.01	0.12	0.09	0.32	0.52	0.00	0.00	0.07	0.10	0.00	0.00	0.00	0.00
CaO	n.a.	n.a.	0.00	0.00	0.06	0.10	0.01	0.01	0.01	0.01	0.00	0.00	0.01	0.01	0.01	0.01	0.01	0.01	0.01	0.00
Na_2O	n.a.	n.a.	0.17	0.02	0.01	0.01	n.a.	n.a.	0.01	0.01	0.00	0.00	0.01	0.01	0.00	0.01	0.02	0.02	0.01	0.02
K_2O	n.a.	n.a.	0.00	0.00	0.06	0.12	n.a.	n.a.	0.01	0.01	0.00	0.00	0.01	0.01	0.01	0.01	0.01	0.00	0.00	0.00
H_2O					12.45	0.15														
Total	99.12	0.84	99.58	0.32	99.8	1.4	100.21	0.62	99.02	1.07	100.28	0.95	100.86	0.43	100.43	0.21	101.46	0.20	101.31	0.37
Zr ppm	192	184	225	184	217	209			112	129	278	236	911	357	580	318	527	182	35	61
Si (*apfu*)	0.05	0.15	0.00	0.00	2.44	0.20	0.00	0.00	0.00	0.00	0.00	0.00	0.00	0.00	0.00	0.00	0.00	0.00	0.00	0.00
Ti	0.96	0.05	0.00	0.00	0.01	0.01	1.94	0.02	0.97	0.02	0.01	0.01	0.99	0.00	0.99	0.00	0.99	0.00	0.98	0.00
Zr	0.00	0.00	0.00	0.00	0.00	0.00	1.03	0.02	0.00	0.00	0.00	0.00	0.00	0.00	0.00	0.00	0.00	0.00	0.00	0.00
Al	13.92	0.21	1.85	0.00	3.14	0.32	n.a.	n.a.	0.00	0.00	0.08	0.13	0.00	0.00	0.00	0.00	0.00	0.00	0.00	0.00
Cr	0.23	0.06	0.08	0.00	0.02	0.02	0.00	0.00	0.00	0.00	0.02	0.01	0.00	0.00	0.00	0.00	0.00	0.00	0.00	0.00
Fe3	1.81	0.13	0.07	0.00	0.00	0.00	0.03	0.01	0.00	0.00	1.86	0.16	0.01	0.00	0.01	0.00	0.00	0.00	0.02	0.00
Fe2	1.69	0.28	0.41	0.00	0.65	0.13	0.00	0.00	1.04	0.04	0.99	0.02	0.00	0.00	0.00	0.00	0.00	0.00	0.00	0.00.
Mn	0.01	0.00	0.00	0.00	0.00	0.00	0.00	0.00	0.01	0.00	0.00	0.00	0.00	0.00	0.00	0.00	0.00	0.00	0.00	0.00

(Continues)

TABLE 1 (Continued)

	Högbomite		Spinel		Chlorite		Srilankite		Ilmenite		Magnetite		Rutile (coarse)		Rutile next to Hög		Rutile rimming Chl		Rutile symplectitic	
Mineral analyses	***n* = 30**	**1 s.d.**	***n* = 6**	**1 s.d.**	***n* = 8**	**1 s.d.**	***n* = 4**	**1 s.d.**	***n* = 9**	**1 s.d.**	***n* = 4**	**1 s.d.**	***n* = 10**	**1 s.d.**	***n* = 3**	**1 s.d.**	***n* = 5**	**1 s.d.**	***n* = 4**	**1 s.d.**
Zn	0.60	0.10	0.16	0.00	0.00	0.00	0.00	0.00	0.00	0.00	0.01	0.01	0.00	0.00	0.00	0.00	0.00	0.00	0.00	0.00
Ni	n.a.	n.a.	0.00	0.00	0.00	0.00	n.a.	n.a.	n.a.	n.a.	n.a.	n.a.	n.a.	n.a.	n.a.	n.a.	n.a.	n.a.	n.a.	n.a.
Mg	2.71	0.25	0.43	0.00	3.70	0.12	0.00	0.00	0.00	0.00	0.02	0.03	0.00	0.00	0.00	0.00	0.00	0.00	0.00	0.00
Ca	n.a.	n.a.	0.00	0.00	0.01	0.01	0.00	0.00	0.00	0.00	0.00	0.00	0.00	0.00	0.00	0.00	0.00	0.00	0.00	0.00
Na	n.a.	n.a.	0.01	0.00	0.00	0.00	n.a.	n.a.	0.00	0.00	0.00	0.00	0.00	0.00	0.00	0.00	0.00	0.00	0.00	0.00
K	n.a.	n.a.	0.00	0.00	0.01	0.01	n.a.	n.a.	0.00	0.00	0.00	0.00	0.00	0.00	0.00	0.00	0.00	0.00	0.00	0.00
Cation Σ	22.00	0.00	3.00	0.00	8.00	0.00	3.01	0.003	2.03	0.02	3.00	0.00	1.00	0.00	1.00	0.00	1.00	0.00	1.01	0.00
$X_{Mg} = Mg/(Mg+Fe^{2+})$	0.62		0.51		0.85															
$Y_{Cr} = Cr/(Cr+Al+Fe^{3+})$	0.01		0.04		0.01															
$X_{Fe} = Fe^{3+}/(Fe^{2+}+Fe^{3+})$	0.52		0.14		0.00															

Abbreviations: apfu, atoms per formula unit; n.a., not analyzed.

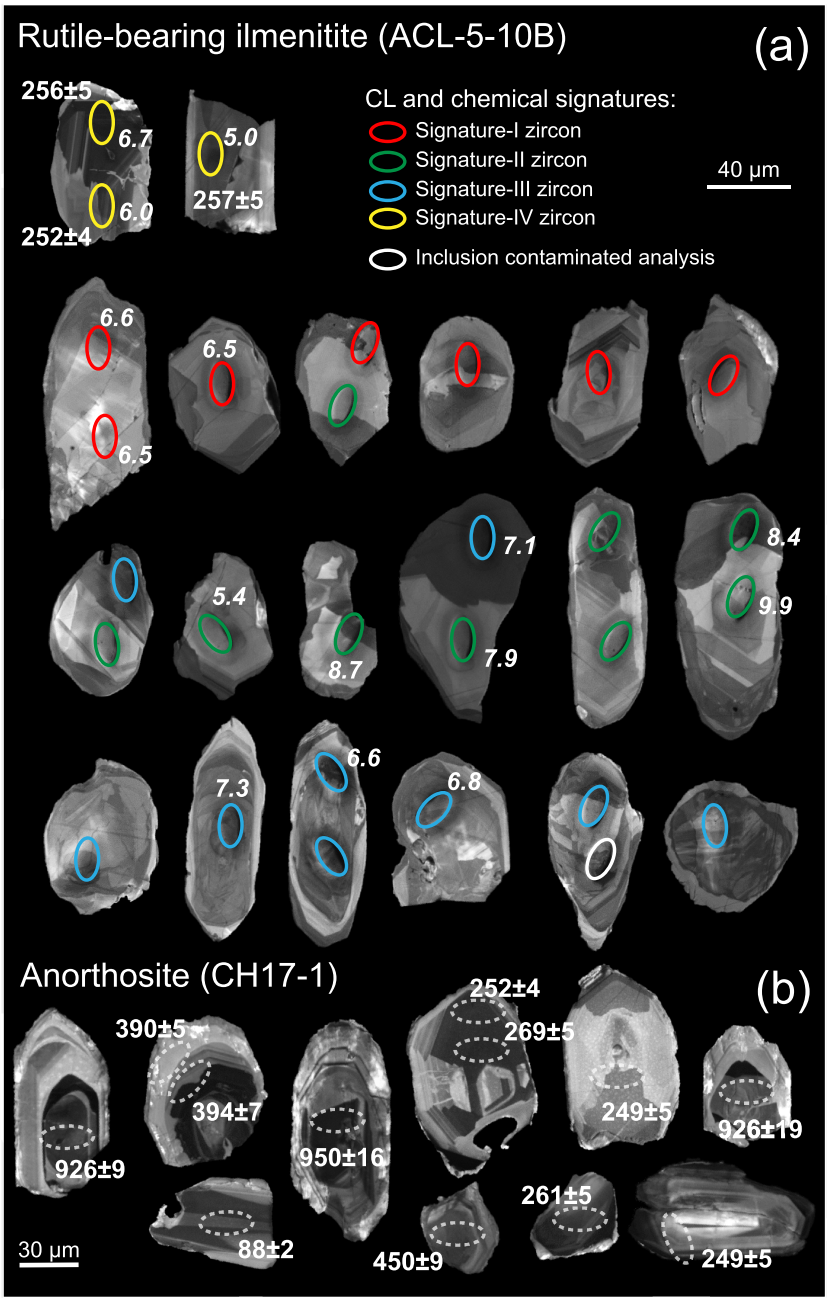

FIGURE 8 Cathodoluminescence (CL) images of analysed zircon grains from rutile-bearing ilmenitite (ACL-5-10B) and anorthosite (CH17-1). (a) Rutile-bearing ilmenitite zircon with colour ellipses representing analysed areas for age and trace elements; $\delta^{18}O$ values are also indicated where available. The colour of ellipses represents zircon chemical signatures defined by similar rare earth element (REE) chemistry patterns. Numbers are ^{238}U-^{206}Pb ages in Ma and errors are 1σ, whereas italic numbers represent $\delta^{18}O$ values in ‰ (error is 0.28‰). (b) Anorthosite zircon CL images with U–Pb spot location as dashed ellipse.

also depicted in Figures 3–6. Zircon separates show complex internal CL domains usually comprising CL-light, homogeneous and irregularly shaped cores overgrown by CL-darker rims. Rims are usually constituted of fine zircon growth increments that give a laminated or banded aspect to the crystals but that are dissimilar to typical oscillatory zonation. However, there is also a zircon population dominated by dark cores and thin brighter rims. Dark cores exhibit highly complex internal structures composed of chaotic growth.

Chondrite-normalized REE patterns (Figure 9a–d) from zircon separates of the RBI (ACL-5-10B; Table S2) indicates at least four distinguishable chemical signatures (CS) in zircon. In general, all chemical signatures are characterized by patterns with enriched HREE and depleted LREE, but total REE and middle rare earth elements (MREE) to HREE patterns vary between the distinct chemical signatures. Zircon crystals from CS-I show slight concave MREE to HREE patterns (Figure 9a), whereas CS-II zircon is characterized by flat MREE patterns (Figure 9b). The CS-III zircon shows a steady increase from MREE to HREE concentrations (Figure 9c), whereas the CS-IV zircon (c. 250 Ma, see geochronology section) has an overall higher MREE to HREE concentration (Figure 9d), displaying also slightly to moderate concave patterns. Due to the occurrence of

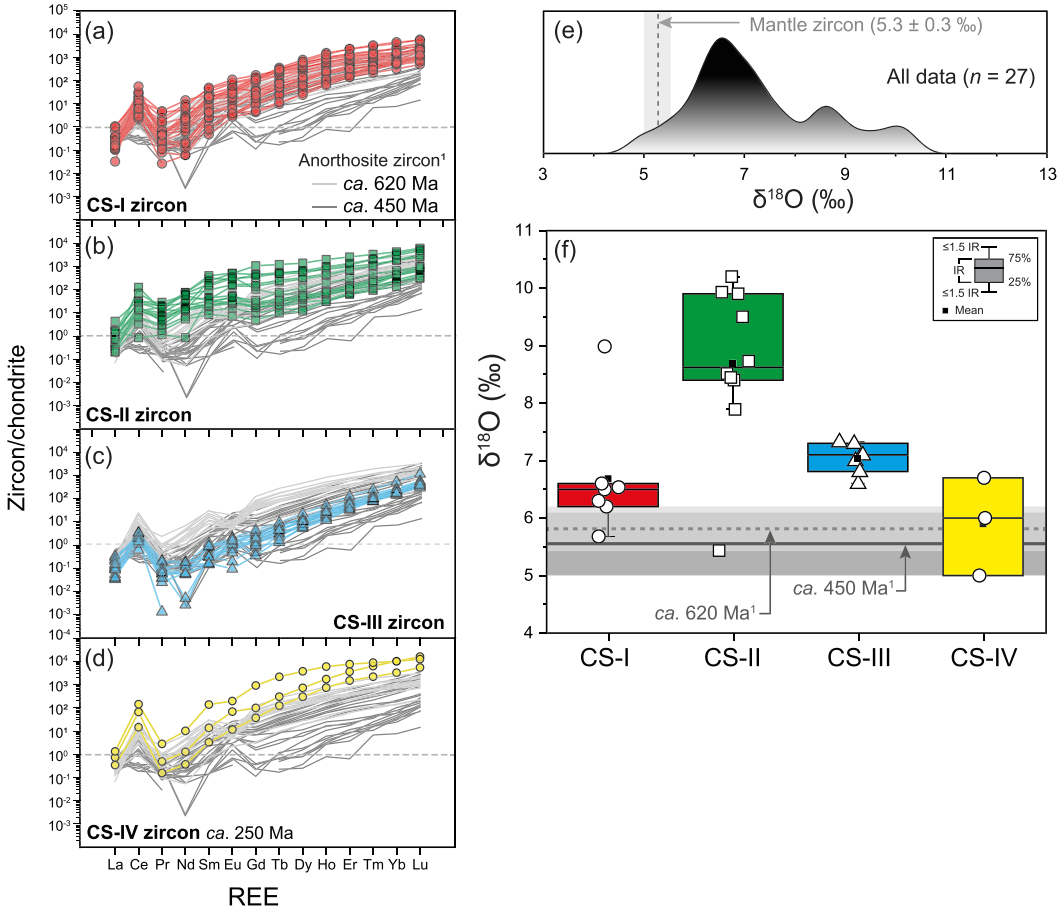

FIGURE 9 Trace element and oxygen isotope compositions of zircon from RBI (ACL-5-10B). (a–d) Chondrite-normalized rare earth element (REE) patterns from zircon of the rutile-bearing ilmenitite (RBI) and comparison with zircon from associated anorthosites. Chondrite-normalized zircon REE patterns were split into distinct chemical signature classes; the dashed line is plotted as a reference for ~0.2 ppm concentration. (e) Probability–density function for all oxygen isotope compositions from zircon of the RBI. (f) Oxygen isotope composition box plots for zircon of the RBI separated into distinct chemical signatures classes; [1]Ediacarán and Ordovician zircon lines represent $\delta^{18}O$ zircon averages (solid and dashed lines) and corresponding standard deviations (grey bands) from neighbouring anorthosites studied by Weber et al. (2020).

sporadic outlier values that may strongly bias zircon chemical results, we use the statistical median instead of average to express representative concentrations hereafter. The U contents in CS-I, -II and -III zircon are unusually low, with median values ranging from 0.1 to 0.9 ppm (Figure 10a). This strongly contrasts with comparatively high-U contents in CS-IV zircon (220–2510 ppm). The Th abundances are in general extremely low as well (0.9–3.4 ppm), except for the CS-IV zircon (768 ppm; Figure 10b). Whereas values for Hf are relatively similar between all chemical signatures (10,647–13,635 ppm), Y shows differing values that decrease in the following order: CS-IV (3132 ppm), CS-I (556 ppm), CS-II (106 ppm) and CS-III (22 ppm). The ΣREE is also significantly variable between distinct chemical signatures zircon and decreases in the order of CS-IV (3157 ppm), CS-I (400 ppm), CS-II (206 ppm) to CS-III (58 ppm; Figure 10). A similar order also holds for HREE (e.g., Lu and Yb); however, for the LREE and MREE (e.g., La, Ce and Pr), comparatively elevated elemental concentrations are characteristic for CS-IV and CS-II zircon. Both negative and positive Eu/Eu* anomalies (with Eu* calculated from the geometric mean of chondrite-normalized Sm and Gd) are observed in the CS-IV and CS-I and -III zircon, whereas CS-II is dominantly represented by positive anomalies (Figure 10d). The Ce/Ce* anomalies are also distinct between chemical signatures; CS-IV zircon displays the largest positive anomalies (median = 74), whereas CS-II has the smallest (median = 6). CS-I and -III zircon crystals have similar Ce/Ce* median values of ~27. Altogether, distinct chemical signature zircon defines positive trends in U, Th and Ti against ΣREE

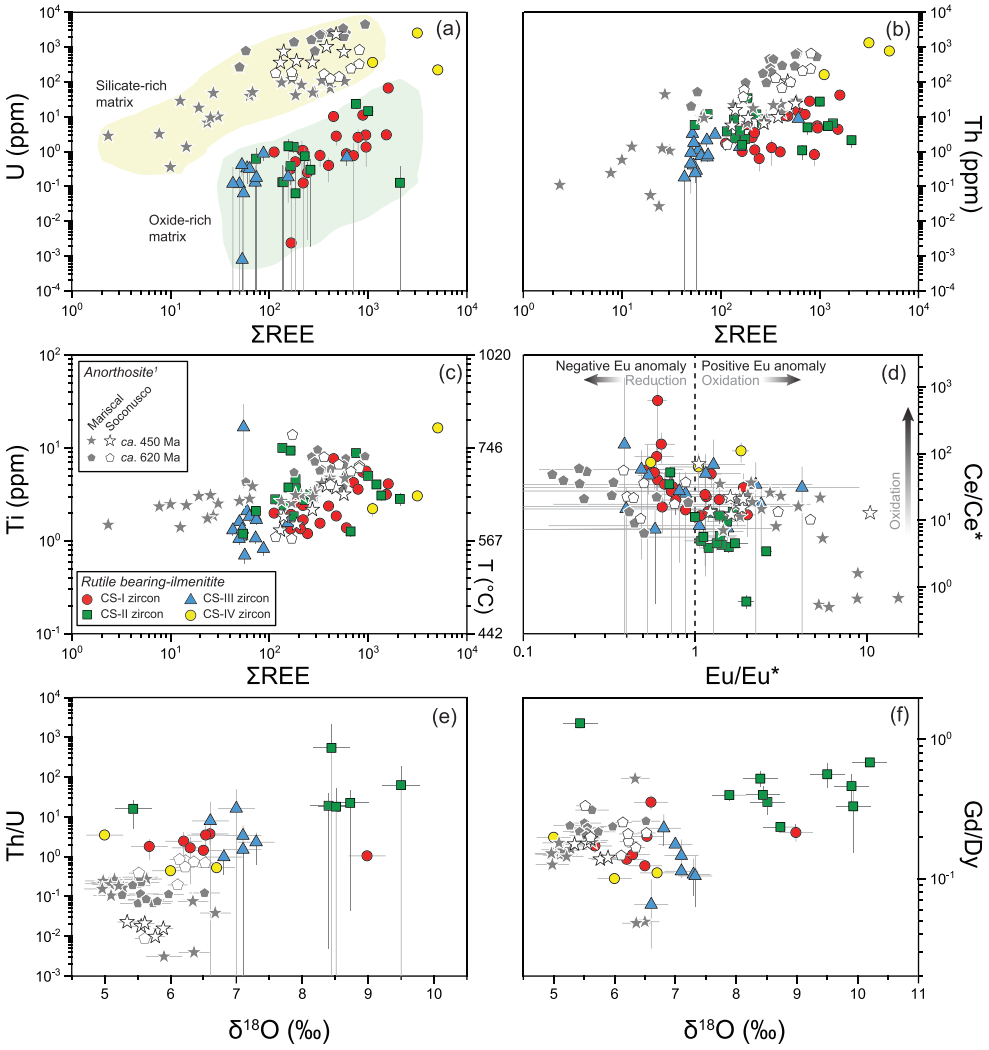

FIGURE 10 Comparison of trace element compositions from zircon of the rutile-bearing ilmenitite (ACL-5-10B) and zircon compositions from comagmatic anorthosites. (a–c) U, Th, Ti plotted against total rare earth element (REE) abundances. (e) Cerium anomalies (Ce/Ce*) versus europium anomalies (Eu/Eu*). (e-f) Th/U and Gd/Dy plotted against oxygen isotope compositions. [1]Ediacarán and Ordovician zircon from neighbouring anorthosites studied by Weber et al. (2020). Error bars are 1σ.

(Figure 10a–c), in which CS-IV zircon occurs as the upper end-member and CS-III zircon as the lower end-member; CS-I and -II zircon overlap at intermediate values. In a hydrothermal zircon discrimination diagram of Hoskin (2005) based on trace elements, all zircon crystals fall outside the hydrothermal field (Figure S4).

4.4 | Oxygen isotopes in zircon

Different CL domains of zircon from the RBI (ACL-5-10B) were targeted to constrain the entire zircon $\delta^{18}O$ compositional spectrum (Table S3). Overall, zircon $\delta^{18}O$ values range from +5.0 to +10.2‰. A probability–density function curve of the entire data set ($n = 26$) suggests three major $\delta^{18}O$ populations at around +6.5, +8.5 and +10.0‰ (Figure 9e). These $\delta^{18}O$ populations partly match the differences observed between distinct zircon chemical signatures (Figure 9f). The CS-I zircon shows an average of 6.5 ± 1.0‰ (1 standard deviation; s.d.); CS-II and -III zircon present averages of 8.5 ± 1.5 and 7.0 ± 1.4‰, respectively, whereas CS-IV zircon shows an average of 5.9 ± 0.7‰. These $\delta^{18}O$ values show a positive correlation with some elemental ratios and differentiation indices, for instance, Th/U and Gd/Dy (Figure 10e,f).

4.5 | Zircon and rutile thermometry

4.5.1 | Ti-in-zircon thermometry from RBI (ACL-5-10B)

Zircon apparent crystallization temperatures ($aTiO_2$ and $aSiO_2 = 1$) for the overall suite of crystals in the RBI range from ~545 to ~797°C ($n = 56$; Figure 11a and Table S2). Probability–density functions indicate a polymodal distribution peaking at ~600, ~730 and ~790°C,

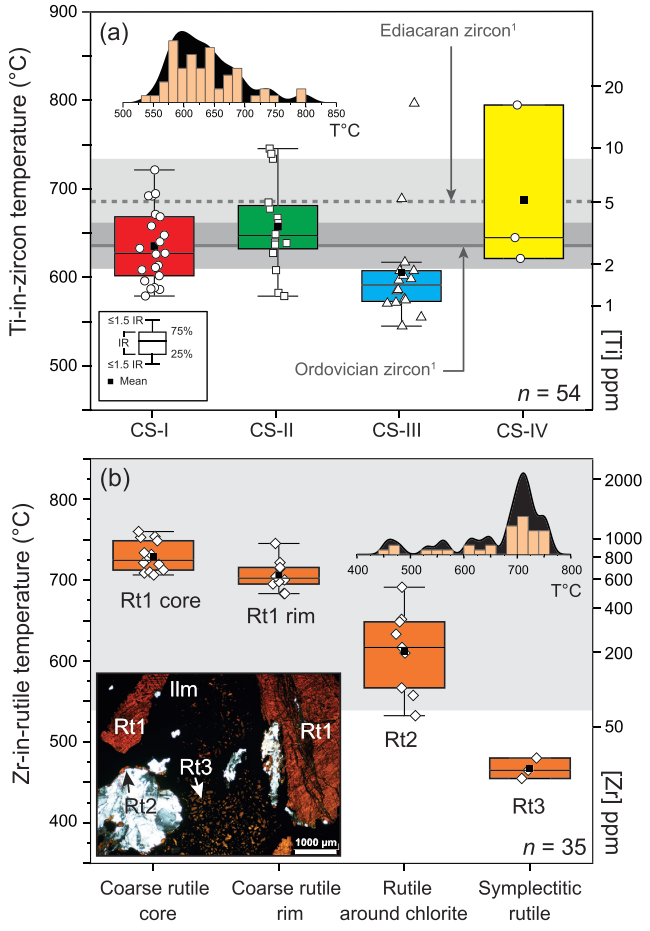

FIGURE 11 Thermometry box plots. (a) Ti-in-zircon thermometry from different chemical signature zircon classes from the rutile-bearing ilmenitite (RBI). Horizontal solid and dashed lines represent average zircon temperatures and standard deviation (grey bands) from Weber et al. (2020) (b) Zr-in-rutile thermometry from all rutile textures observed in the RBI. The grey area represents the 541–1015°C range of Zr-in-rutile temperatures obtained for the same sample by LA-ICPMS (Adame-Martínez et al., 2020).

but averages of individual chemical signatures overlap within one standard deviation. CS-I zircon ranges in temperatures from 579 to 721°C with an average of 635 ± 41°C ($n = 21$); CS-II zircon ranges from 579 to 746°C with an average of 657 ± 49°C ($n = 16$); CS-III shows the lowest temperatures on average, ranging from 545 to 797°C (average = 605 ± 59°C; $n = 16$), and CS-IV shows a range from 621 to 795°C (average = 687 ± 77°C; 1 s.d.; $n = 3$). Varying $aSiO_2$ to lower values (e.g., 0.5) decreases the calculated temperature by an average of ~50°C (see Table S2); however, the relative temperature differences between distinct chemical signatures are preserved.

4.5.2 | Zr-in-rutile thermometry from RBI (ACL-5-10B)

Coarse-grained rutile shows on average the highest Zr concentrations from all textures (spot locations in Figure S5), ranging from 483 to 1085 ppm, which translates into temperatures of 683–760°C, respectively (average = 719 ± 21°C; 1 s.d.; $n = 23$; Figure 11b and Table S4). A systematic rimward decrease in Zr concentrations was observed in all coarse rutile grains (Figure 11b); concentration differences between core and rim can vary from tens to hundreds of ppm in single grains. On average, cores from coarse-grained rutile crystals show slightly higher average temperatures (~730°C) than rims (~706°C; Figure 11b). Although less precise, Zr line profiles over coarse-grained rutile crystals show rimward decreasing concentrations (Figure 12 and Table S1). Rutile rimming chlorite lenses, in general, yielded comparatively low Zr concentrations and Zr-in-rutile temperatures of 532–690°C (63–528 ppm Zr) with an average of 611 ± 48°C ($n = 9$). On the other hand, symplectitic rutile records the lowest Zr concentrations in the sample (19–26 ppm) and therefore the lowest temperatures (454–479°C; $n = 3$). Probability–density functions from the entire suite of rutile textures show a polymodal distribution, with major population peaks occurring at ~460, ~550, ~630 and ~710°C. The temperature difference observed when using alternative Zr-in-rutile thermometer calibrations (e.g., Tomkins et al., 2007) is negligible when assuming a pressure of 9 kbar and around ~10°C difference when assuming 6 kbar (Table S4).

4.6 | Zircon U–Pb geochronology

4.6.1 | Mariscal anorthosite (CH17-1)

Zircon crystals from the anorthosite exhibit rounded to semiprismatic forms and range from 30 to 100 μm in length. CL imaging reveals generally darker cores with homogeneous to patchy-cloudy zoning patterns (Figure 8b). Cores show clear signs of dissolution and are discordantly overgrown by mantle domains with oscillatory or sector-zoned patterns. Mantle domains usually grade rimwards into thicker and more complex domains composed of brighter and broad-banded CL zoning. The textural complexity observed in CL is reflected in the wide semicontinuous spread of concordant ages observed in the concordia diagram (Figure 13a), with $^{206}Pb/^{238}U$ and $^{207}Pb/^{206}Pb$ dates ranging from 1009 ± 52 Ma to 88 ± 2 Ma (1σ; $n = 50$; Table S5). The age probability–density function suggests multiple zircon age distribution

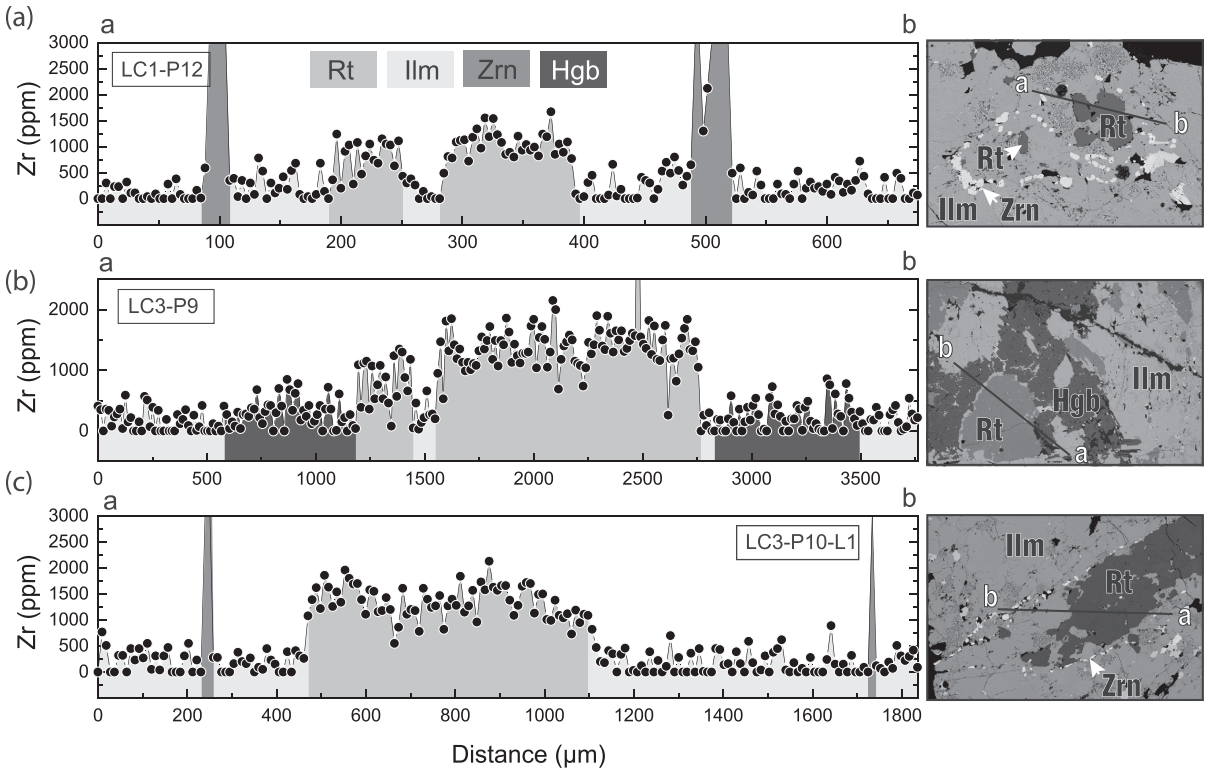

FIGURE 12 *In situ* zirconium concentration electron microprobe (EMP) line profiles across different spatially associated minerals (e.g., rutile, ilmenite, hogbomite and zircon) in the rutile-bearing ilmenitite (RBI) (ACL-5-10B). Different scales of grey represent different minerals.

peaks between c. 950 and 100 Ma (inset Figure 13a). Applying the TuffZirc algorithm (Ludwig, 2003) to obtain the likely age of the two most prominent crystal populations yields dates of 953 $^{+54}/_{-23}$ Ma (2σ; $n = 9$) and 253 $^{+4}/_{-5}$ Ma (2σ; n = 24; Figure 13a). Uranium contents from the whole set of zircon crystals range from 18 to 7486 ppm, in which the c. 250 Ma crystals show on average higher U contents (average of ~500 ppm) and relatively low Th/U ratios (average = 0.2; except for one crystal of c. 450 Ma age showing a ratio of 0.04), whereas the oldest zircon crystals (>800 Ma) show lower U concentrations with an average of ~200 ppm and higher Th/U ratio average of 0.43.

4.6.2 | Rutile-bearing ilmenitite (ACL-5-10B)

From a total of 53 analyses, only three analyses performed in two zircon crystals yielded sufficient U (~220 and ~2510 ppm; Tables S5 and S6) to calculate concordant and reliable dates. These two zircon crystals (Figure 8a) show oscillatory-like zonation at the cores with clear signs of recrystallization at the rims and have overlapping $^{206}Pb/^{238}U$ dates between 252 ± 4 and 257 ± 5 Ma (1σ; Table S5). The rest of the zircon crystals are extremely depleted in U (median = 0.4 ppm; $n = 53$; see Table S6), which is impractically low for geochronology. In order to calculate a geologically significant age from these low-U zircon crystals and avoid potential overcorrection of high common Pb/low-radiogenic Pb analyses, the data were plotted in a Tera–Wasserburg diagram where a linear regression of common Pb-uncorrected data produced a lower intercept age of 256 ± 7 Ma (2σ; $n = 26$; MSWD = 0.49; Figure 13b). A few zircon analyses plot off the regression line.

4.6.3 | Oxide-apatite-rich amphibolite (NF1302)

Zircon crystals from OARA were dated within their textural and mineralogical context (*in situ*; $n = 7$) and as separates (*ex situ*; $n = 20$). Most of the *in situ* dated zircon crystals occur along ilmenite boundaries (Figure 7) and show rounded edges and elongated external morphologies that range in length from just a few μm up to 120 μm. Boudinaged and fragmented grains (especially from large crystals) provide evidence of intense plastic to

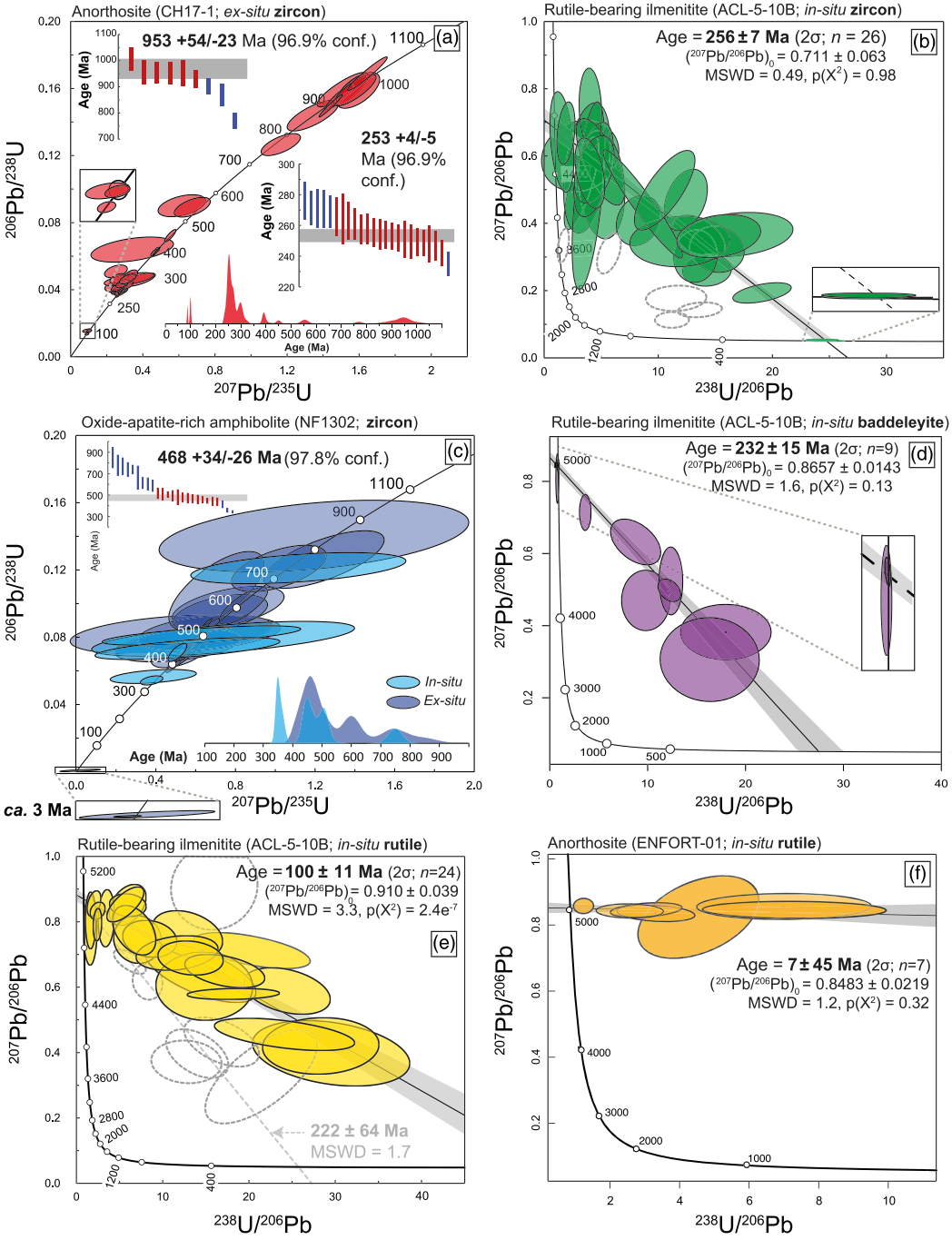

FIGURE 13 Wetherill and Tera–Wasserburg concordia diagrams for secondary ion mass spectrometry (SIMS)-dated accessory minerals (e.g., zircon, baddeleyite and rutile). (a) Zircon dates from anorthosite outcropping near Motozintla. (b) Regression line through common Pb-uncorrected data for undifferentiated zircon from rutile-bearing ilmenitite (RBI) sample. (c) *In situ* and ex situ dates from zircon of the OARA. (d–f) Baddeleyite and rutile analyses with regression lines through common Pb-uncorrected data in Tera–Wasserburg diagrams. Insets in (a) and (c) show probability–density functions based on $^{206}Pb/^{238}U$ age and ages extracted applying the TuffZirc algorithm of Ludwig (2003). Error ellipses are 2σ. Age labelled on the Concordia curve is in Ma. Grey-dashed ellipses were not further considered for age regression calculations; where possible an age regression was calculated separately from the main data trend. MSWD = mean squared weighted deviation.

brittle deformation (Figure 7a–d). Although intragrain deformation is not observable in the BSE images, CL reveals low emission zones that follow internal zircon deformation (dislocation) microstructures (Figure 7b). Overall CL intensity varies between individual grains and fragments. Zircon was also observed within anorthosite microlenses (0.5–1 cm) hosted in the OARA (Figure 7e–f). These grains usually show semiprismatic

shapes and occur as clusters next to ilmenite partly replaced by titanite (Figure S6). Compared with zircon occurring along ilmenite boundaries, zircon in the anorthosite micro-inclusion matrix shows concentric CL zonation, where CL-dark cores are usually overgrown by CL-bright domains (Figure 7e–f and S6). The $^{206}Pb/^{238}U$ *in situ* dates for zircon from OARA range from 738 ± 22 to 342 ± 7 Ma (Figure 13c; 1σ; Table S5; $n = 7$). U contents are in the range of 17 to 593 ppm. Although *in situ* analyses are limited in number, we found no systematic age differences between zircon along ilmenite grain boundaries and those within the anorthosite micro-inclusion matrix. However, U abundances are notably different; zircon from the anorthosite micro-inclusion matrix displays much higher U contents (449–593 ppm) than those analysed at the border of ilmenite (17–146 ppm). Zircon separates contain mostly small (30–60 μm) and CL homogeneous crystals, except for two relatively large (~100 μm) semiprismatic crystals. The $^{206}Pb/^{238}U$ dates for all zircon separates ($n = 20$) range from 849 ± 49 to 3.3 ± 0.5 Ma (1σ; Figure 13c). Most of the crystals have U content that range from 11 to 277 ppm, except for one grain with a U abundance of 1194 ppm. From gathering all dated crystals (*in situ* and *ex situ*), we observed a dominant Ordovician group of zircon crystals that yield a TuffZirc date of 468 $^{+34}/_{-26}$ Ma (97.8% c.i.; $n = 23$), whereas most low-U and CL homogeneous zircon crystals show older ages. Two small and highly bright CL zircon yielded much younger apparent ages of 4.3 ± 1.8 and 3.3 ± 0.5 Ma.

4.7 | Baddeleyite U–Pb ages

4.7.1 | Rutile-bearing ilmenitite (ACL-5-10B)

Due to the common replacement of baddeleyite by zircon and other Zr-rich phases in the RBI, most baddeleyite crystals were too small (<10 μm) to be analysed without sampling adjacent phases. To overcome potential matrix effects due to beam overlapping with such replacing phases (e.g., zircon or srilankite), we targeted only baddeleyite crystals with negligible signs of secondary alteration (see Figure 5e–f). All dated baddeleyite grains show homogeneous CL intensities that are overall darker than those of zircon (Figure 5h). All nine analysed baddeleyite crystals yielded extremely low-U signals (Table S7), hampering reliable single-grain age calculation. Nevertheless, linear regression combining all common Pb-uncorrected data in a Tera–Wasserburg diagram (Figure 13d) yielded a lower intercept age of 232 ± 15 Ma (2σ; MSWD = 1.6; $n = 9$) and a *y*-axis intercept indicating common $^{207}Pb/^{206}Pb = 0.87$ for the population.

4.8 | Rutile U–Pb ages

4.8.1 | Rutile-bearing ilmenitite (ACL-5-10B)

Rutile crystals were dated *in situ* and targeted based on their textures (e.g., coarse-grained). Regardless of their texture, all analysed rutile grains had very low U abundances (<1 ppm; Table S8), hampering single grain age calculation. However, as with baddeleyite, a lower intercept model age was obtained by regression through data uncorrected for common Pb in a Tera–Wasserburg concordia diagram. Regardless of rutile texture, almost all data fall on the same trend and are therefore considered potentially as a single population with variable proportions of common and radiogenic Pb. The lower intercept age defined by most analyses is 100 ± 11 Ma (2σ; MSWD = 3.3; $n = 24$; Figure 13e). The large MSWD hints at more than a single rutile population in the data. A few grains preserve evidence of inheritance (grey circles); for these, linear regression yields a lower intercept age of 222 ± 64 Ma (2σ; MSWD = 1.7; $n = 6$).

4.8.2 | Mariscal anorthosite (ENFORT-01)

Rutile coronas around ilmenite grains within the anorthosite near Acacoyagua (Figure 2d–e) yielded a regression line through uncorrected data that has a very young lower intercept age of 7 ± 45 Ma (2σ; MSDW = 1.2; $n = 7$; Figure 13f), indicating no significant accumulation of radiogenic lead in this rutile (Table S8).

5 | DISCUSSION

5.1 | The formation of Zr-bearing phases through diffusion

The formation of secondary baddeleyite and zircon has been frequently reported for igneous and metamorphic rocks associated with different Zr-bearing minerals like ilmenite and rutile (Beckman et al., 2017; Bingen et al., 2001; Charlier et al., 2007; Morisset & Scoates, 2008). The partitioning of Zr into these minerals during crystallization is permissible due to similar ionic radii of Ti^{4+} (0.61 Å) and Zr^{4+} (0.72 Å; Shannon, 1976; Zack, von Eynatten, et al., 2004) at the same charge, and Zr incorporation into högbomite may proceed similarly. The kinetic expulsion of Zr (granular exsolution) from high-Zr parental phases is usually attributed to lower Zr solubility in the lattice of Ti-Fe oxides, attained either during slow magmatic or metamorphic cooling (Bingen et al., 2001) or complete mineral breakdown

(e.g., garnet; Degeling et al., 2001). Whether exsolved ZrO_2 transforms directly into zircon may strongly depend on the local availability of silica during post-magmatic cooling or subsequent metamorphism (Beckman et al., 2014, 2017; Bingen et al., 2001; Davidson & Van Breemen, 1988; Morisset & Scoates, 2008).

5.1.1 | Baddeleyite

The ubiquitous presence of pristine baddeleyite grains and relicts within Zr-bearing phases (Figures 3–6) in close spatial association with both magmatic and metamorphic minerals (e.g., ilmenite, rutile and högbomite; Figures 2–6) suggests that baddeleyite in the RBI originated episodically from subsolidus external exsolution during either slow magmatic cooling or during cooling of any of the multiple metamorphic events experienced by the RBI, or both (e.g., Bingen et al., 2001; Charlier et al., 2007; Morisset & Scoates, 2008). Multi-episodic formation of baddeleyite is further supported by the textural evidence of baddeleyite transforming into distinct Zr-bearing phases (e.g., srilankite, zircon and zirconolite), which likely reflects distinct conditions/timing of formation/replacement of the precursor baddeleyite crystals. Further support to the multi-episodic formation of baddeleyite besides the presence of baddeleyite relicts in all different zircon types is the significantly younger U–Pb age (e.g., 232 ± 15 Ma; Figure 13d) for pristine baddeleyite grains (Figure 5e-h) relative to the estimated crystallization age of the anorthosite suite at c. 1.01 Ga.

5.1.2 | Type-I zircon

T*ype-I* zircon occurs as overgrowths on srilankite crystals formed after baddeleyite within ilmenite interstices in the RBI (Figure 3). Srilankite occurs exclusively in the RBI and is genetically associated with baddeleyite that exsolved from both ilmenite and högbomite during magmatic cooling according to the textural record (Figures 3 and 4). To understand the formation of *type-I* zircon after srilankite, it is necessary to consider srilankite formation in this geological context.

Srilankite has been usually found spatially associated with Ti-Fe oxides in high-grade metamorphic rocks like eclogites and granulites (Bingen et al., 2001; Jiao et al., 2011; Wang et al., 1999), although direct exsolution from ilmenite or a magmatic origin has also been suggested from gabbroic dykes within ophiolite sequences (Morishita et al., 2004; Pujol-Solà et al., 2020). Experimental studies point to a formation of srilankite in equilibrium with rutile at high pressures and temperatures, at least under oxidizing conditions (>1150°C and >15 kbar; Troitzsch et al., 2005; Troitzsch & Ellis, 2004; Troitzsch & Ellis, 2005). However, Troitzsch and Ellis (2004) caution that other factors should be considered during the formation of srilankite, as the incorporation of elements like Sn and Fe as well as fluid pressure could have an influence on the stability of srilankite at natural conditions. The intimate relationship of srilankite with haematite (Figure 3) may also suggest suitable oxidizing conditions for its formation, as Fe_2O_3 ensures buffering of high oxygen fugacities during the srilankite formation process (e.g., Troitzsch & Ellis, 2004).

We suggest that srilankite in the RBI formed coevally with coarse-grained rutile after reaction of baddeleyite with a parental ilmenite precursor (e.g., Bingen et al., 2001) during the first and highest-grade metamorphic event experienced by the RBI. The minimum estimated peak metamorphic temperature for this event ranges between ~700°C and 750°C based on Zr-in-rutile thermometry of coarse-grained rutile (acknowledging post-crystallization Zr diffusion), whereas the timing could be correlated to the first metamorphic zircon population in the anorthosite sample dating to 950 $^{+54}/_{-23}$ Ma (Figures 14 and 15). This date overlaps with the c. 940–960 Ma metamorphic event that promoted anatexis in rocks of the Candelaria and Catarina unit (e.g., Valencia-Morales et al., 2022; Weber et al., 2018) but is also similar within uncertainty to the c. 990 Ma granulite facies event recorded in anorthosites elsewhere in Mexico (Solari et al., 2003, 2004). Potential support for srilankite formation during high-grade metamorphism is the presence of rutile inclusions (Figure 3a–e), which is also a common characteristic in rare garnet in the same sample (Figure 2m). Other generations of rutile of lower temperature, however, are also present, likely reflecting lower-grade stages of the RBI history or, alternatively, growth of rutile during the final stages of the c. 950 Ma metamorphic overprint. Haematite was likely derived as a by-product of the prograde reaction from ilmenite into rutile but also from the exsolution of haematite lamellae during the cooling of ilmenite. Additional formation of haematite at a later stage of the rock evolution may have also occurred during the oxidation of ilmenite as suggested by the formation of symplectic intergrowths between haematite and low-temperature pseudorutile(?) or leucoxene (?) (~450°C; Figure 11b) in ilmenite interiors (Figures 2g and 3c; Briggs & Sacco, 1993). Remobilization and reprecipitation of haematite formed during any of the above-mentioned mechanisms may have also been associated with haematite pseudomorphic texture after högbomite (Figure 4f).

The timing for *type-I* zircon formation after srilankite is thus necessarily younger than the c. 950 Ma srilankite-

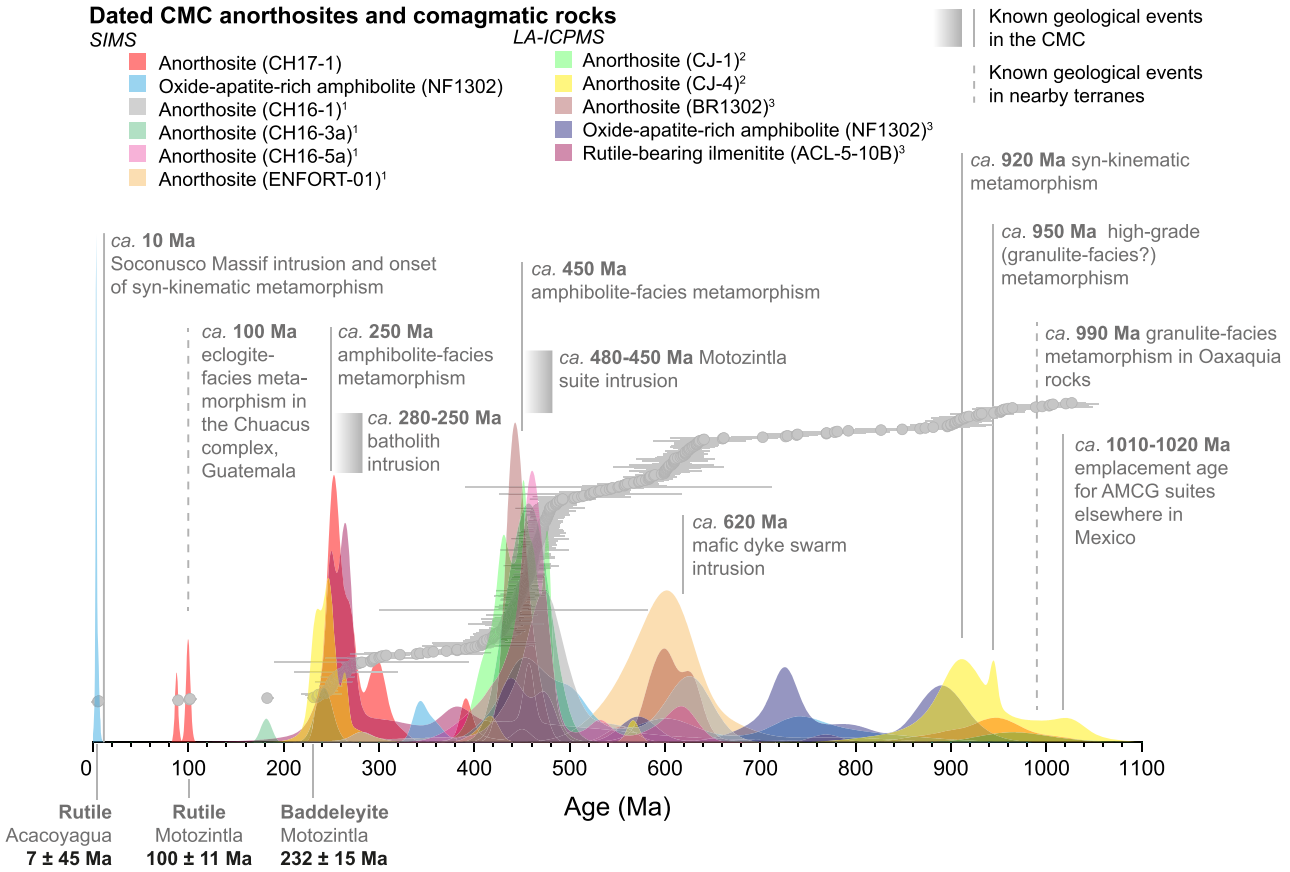

FIGURE 14 Ranked-order zircon crystallization dates (grey circles) and pooled zircon age distributions for anorthosites and comagmatic rocks from this study and Weber et al. (2020)[1], Estrada-Carmona et al. (2012)[2], and Cisneros de León et al. (2017)[3]

forming metamorphic event and could be associated with any combination of the subsequent metamorphic episodes recorded in the region (e.g., c. 920, 620, 450 and 250 Ma; Figures 14 and 15). The evidence of multiple dissolution/growth zones (metamorphic events) within *type-I* zircon interior as shown by CL (Figure 3) is in agreement with multiple, chemical, isotopic and temperature signatures (Figures 9–11) within individual zircon crystals from separates (i.e., lacking textural context; Figure 8a). Therefore, the genesis of *type-I* zircon and likely all other types cannot be uniquely assigned to a single metamorphic event but rather represents a cumulative growth record associated with the multiple stages of the polymetamorphic history in the CMC. Unfortunately, low-U from most zircon crystals in the RBI precluded dating of the different chemical signatures, which hinders further correlation to specific metamorphic events. Nonetheless, all metamorphic episodes are geochronologically well-preserved in the zircon cargo of the RBI-host anorthosite bodies (Estrada-Carmona et al., 2012; Weber et al., 2020) and other comagmatic rocks (e.g., OARA; Figure 14).

5.1.3 | Type-II zircon

Type-II zircon occurs at the borders of ilmenite in contact with chlorite lenses (Figures 2n–o and 5a–d). *Type-II* zircon also preserves baddeleyite relicts and only in exceptional cases srilankite is present (Figure 6c). In some cases, *type-II* zircon is completely enclosed by chlorite lenses, suggesting that zircon remained immobile during subsequent metamorphism and/or metasomatism that caused ilmenite boundary migration (e.g., Austrheim et al., 2008; Figure 2n). The origin of *type-II* zircon could be related to the exsolution of baddeleyite from ilmenite during magmatic cooling and reaction with deuteric silica-rich fluids at the grain boundaries (e.g., Charlier et al., 2007; Heaman & LeCheminant, 1993; Morisset & Scoates, 2008) or by reaction with the neighbouring silicate precursor phase of chlorite (e.g., ferromagnesian mineral; Figure 15). However, the presence of srilankite in this setting requires an explanation. We suggest that some baddeleyite at the borders of ilmenite did not react directly to form zircon shortly after exsolution from the parental phase, likely precluded by the local conditions

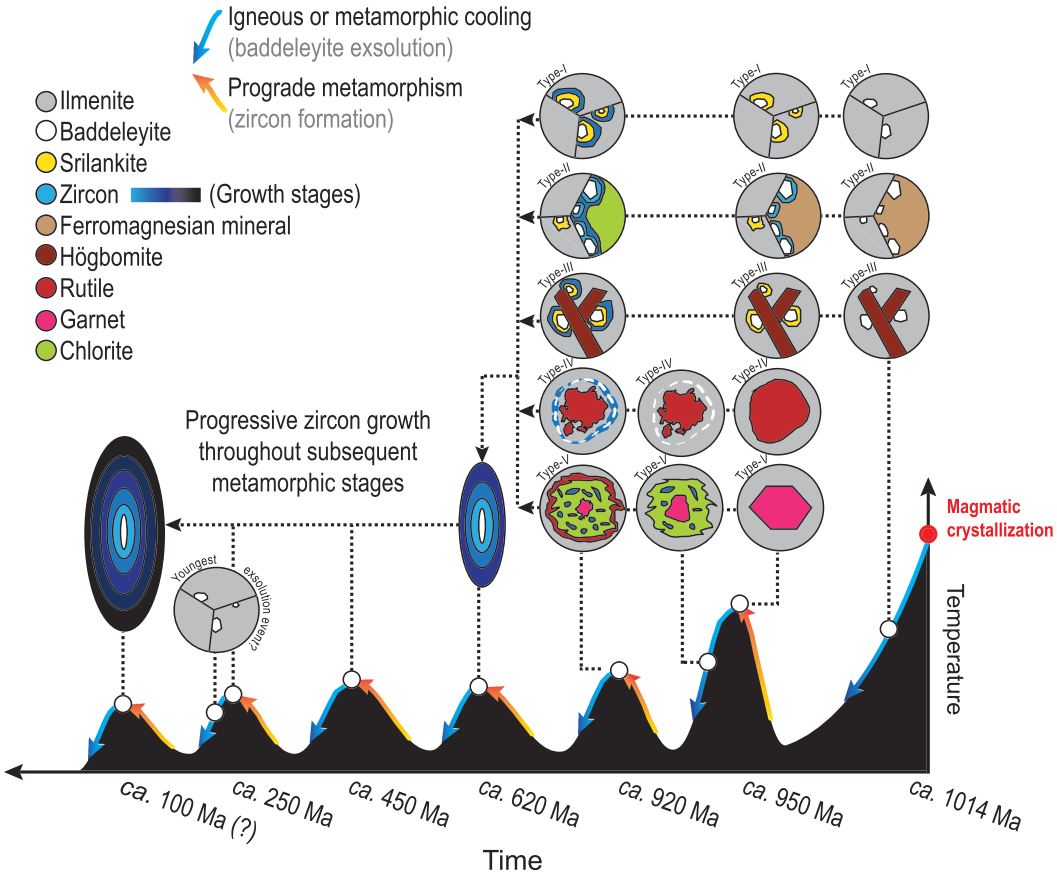

FIGURE 15 Schematic evolution of Zr-bearing phases throughout multiple metamorphic events experienced by the Chiapas Massif Complex

like lower or negligible silica availability or phase shielding (protection against fluids). If so, such pristine baddeleyite grains may have only reacted with neighbouring ilmenite to form srilankite after deformation during peak metamorphism at c. 950 Ma (e.g., Bingen et al., 2001). This would explain the presence of coeval rutile inclusions in both srilankite crystals and *type-II* zircon within the same textural setting. The evidence of complex internal domains in *type-II* zircon also suggests a history of multiple growths and dissolution events. The larger size of *type-II* zircon relative to other types may also suggest an adequate location for enhanced interaction with Si-bearing metamorphic fluids or silicate phases.

5.1.4 | Type-III zircon

Type-III zircon is spatially associated with large prismatic högbomite crystals in the RBI (Figure 4a–d). The formation of högbomite has been associated with a wide spectrum of geological environments including hydrothermal, magmatic and UHT metamorphic rocks (Devaraju et al., 1981; Konzett et al., 2005; Liati & Seidel, 1994; Nishimiya et al., 2009; Perumala & Merkle, 2014; Petersen et al., 1989; Rakotonandrasana et al., 2010; Razakamanana et al., 2000; Visser et al., 1992). Högbomite has been reported from other Ti-Fe deposits around the world (Beura et al., 2009; Devaraju et al., 1981, 2014; Jayaraj et al., 1995; Konzett et al., 2005; Mohanty et al., 1995). However, the conditions and processes of its formation in this particular setting are still unclear. Its genesis is commonly attributed to an igneous origin or complex oxidation-exsolution process of magnetite or spinel breakdown in Ti-Fe oxide deposits (Beura et al., 2009; Devaraju et al., 1981; Grew et al., 1990; Petersen et al., 1989). Högbomite compositions from the RBI are in general similar to other occurrences worldwide (e.g., Beura et al., 2009; Devaraju et al., 1981; Grew et al., 1990; Jayaraj et al., 1995; Liati & Seidel, 1994; Mancktelow, 1981; Mohanty et al., 1995; Petersen et al., 1989; Rakotonandrasana et al., 2010; Sengupta et al., 2009). However, högbomite from the CMC stands out as exceptionally rich in Cr_2O_3 (~1.43 wt %; Figure S1). Titanium is on average slightly lower

(~6.14 wt%) than other Ti-Fe oxide ore-related högbomites (e.g., Beura et al., 2009; Devaraju et al., 1981; Jayaraj et al., 1995; Mohanty et al., 1995) but similar or higher than metamorphic occurrences reported for locations in the United States, Australia and Antarctica (Grew et al., 1990; Mancktelow, 1981; Petersen et al., 1989).

The textural relationship of large prismatic högbomite crystals in the RBI suggests a primary igneous origin (Figure 4), and its preservation was likely enhanced by ilmenite shielding, precluding significant fluid infiltration and transformation into chlorite during metamorphic events. Nonetheless, the second generation of högbomite is present as rims around spinel grains and presumably formed by the reaction of spinel with ilmenite/rutile during high-grade metamorphism (Figure 2l; Petersen et al., 1989). Metamorphic högbomite has distinguishable compositions from that of igneous origin in the RBI, especially in Al_2O_3 and MgO contents (Figure S1) and possibly in Zr content as well, as no baddeleyite nor zircon has been observed associated with secondary högbomite. The magmatic origin of prismatic högbomite and the textural record suggests that associated baddeleyite also formed from the exsolution of Zr during magmatic cooling (Figure 15). The average Zr contents of högbomite are up to ~180 ppm, indicating it is a significant Zr repository within the RBI. Moreover, the positive correlation of Zr and Ti content in some högbomite crystals supports the substitution of Ti^{4+} by Zr^{4+} during crystallization (Figure S1). The evidence of *type-III* zircon preserving baddeleyite and srilankite cores (Figure 4a–d) thus suggests a similar origin of *type-I* zircon driven by the reaction of srilankite with Si-enriched fluids during post-950 Ma metamorphism.

5.1.5 | Type-IV zircon

Type-IV zircon occurs as coronas around coarse-grained rutile or delimiting former borders of coarse-grained rutile now retrogressed into ilmenite or chlorite (Figures 2p–q and 6). This texture suggests that rutile was the parental Zr repository and source for *type-IV* zircon formation. The Zr partitioning and diffusion in rutile have been experimentally constrained (Cherniak et al., 2007; Ferry & Watson, 2007; Tomkins et al., 2007; Zack, Moraes, et al., 2004); however, controversy still exists regarding Zr diffusion rates (Blackburn et al., 2012; Cherniak et al., 2007; Ewing et al., 2013; Kooijman et al., 2012; Luvizotto & Zack, 2009; Meyer et al., 2011; Pape et al., 2016; Taylor-Jones & Powell, 2015; Zack, Moraes, et al., 2004). Cherniak et al. (2007) have shown that rutile is only moderately retentive for Zr, whereas geological studies indicate preservation of Zr-in rutile cores even at UHT (Ewing et al., 2013; Kooijman et al., 2012; Pape et al., 2016; Tual et al., 2018).

In the RBI, diffusion of Zr from rutile is suggested by rimward depletion of Zr contents in all grains independently of whether zircon coronas are present or not (Figures 11 and 12). Similar rimward Zr decreasing zoning patterns have been alternatively explained by dissolution–reprecipitation processes (Ewing et al., 2013; Pape et al., 2016), but the uniform composition of coexisting trace elements (e.g., Cr; Figure S3) in rutile from the RBI conflicts with this interpretation. Estimated average temperatures for the formation of coarse-grained rutile based on Zr-in-rutile thermometry indicates minimum average core temperatures of ~730°C, whereas rims indicate lower average temperatures of ~706°C (Figure 12). Moreover, Zr-in-rutile thermometry from the same RBI sample (ACL-5-10B; Adame-Martínez et al., 2020; LA-ICP-MS) indicates temperatures as high as 1015°C. Recalculating the original Zr content of coarse-grained rutile before Zr external exsolution based on the Pape et al. (2016) approach, we found that original Zr concentrations exceeded 1000 ppm when using a conservative zircon volume of 0.2% relative to its parent rutile grain volume. This translates into Zr-in-rutile temperatures of >800°C. Thus, coarse-grained rutile is presumably associated with a high-T or ultra high-T metamorphic event likely at c. 950 Ma based on its crystallization temperatures but also upon the observation that younger metamafic rocks (e.g., c. 620, 450 and 250 Ma) in the CMC lack rutile in their mineral assemblage. Ti-in-zircon temperatures for grain separates from the RBI indicate on average lower temperatures (545–797°C) for the distinct chemical signature zircon relative to coarse-grained rutile. This supports the potential asynchronous formation of the coexisting rutile and zircon.

We consider that the widespread presence of baddeleyite relicts within *type-IV* zircon, and systematic rimward depletion of Zr in coarse-grained rutile suggests post-crystallization compositional re-equilibration, resulting in external exsolution of ZrO_2 by volume diffusion during slow cooling after the c. 950 Ma metamorphic event (e.g., Bingen et al., 2001; Kooijman et al., 2012; Figure 15). Diffusion modelling of Zr concentrations in two different coarse-grained rutile crystals (350 and 950 μm radius) with similar core temperatures (~790°C; Figure S7) shows contrasting cooling timescales when zircon is associated either with zircon coronas (c. 2 Myr; grain LC3-P10-L1; Figures 12c and S7a) or shielded by högbomite (c. 30–50 Myr; grain LC3-P9; Figures 12b and S7b). However, this could be just an artefact of differences in residence time resulting from the asynchronous

formation of the studied grains, which may be also supported by the significant size difference between them. Alternatively, the short c. 2 Myr timescale could be an artefact of modelling Zr compositions throughout an oblique profile relative to the grain border (Figure 12c). Thus, the c. 30–50 Myr timescale can be considered as a maximum for slow cooling of the coarse-grained rutile during which conditions were suitable for baddeleyite formation from volume diffusion following the c. 950 Ma event. However, we caution that this timescale might be biassed towards longer timescales by the integrated effects of multiple thermal events affecting the same rutile grain. Thus, former baddeleyite coronas around rutile (later transformed into zircon) are likely the second generation formed in the RBI and the first of metamorphic origin. Transformation of baddeleyite into zircon and subsequent episodic growth likely proceeded during the subsequent metamorphic events resulting from the interaction of Si-rich fluids along grain boundaries. The spatial preservation of zircon coronas after consumption of rutile by ilmenite underscores the immobile nature of Zr and the initial interface of reaction (e.g., Austrheim et al., 2008).

5.1.6 | Type-V zircon

Type-V zircon occurs as random accumulations of zircon within chlorite and biotite lenses. This is likely the least frequent texture of zircon in the RBI. Nonetheless, *type-V* zircon contrasts with the rest of zircon textures by presenting tens to hundreds of randomly oriented zircon crystals of different sizes following no ilmenite or rutile boundaries and lacking any baddeleyite relicts (Figure 2r). Based on the presence of garnet (Figure 2m) or högbomite relicts within chlorite lenses (Figures 2k and 4e), we presume that this zircon texture may have derived from the breakdown of a Zr-bearing phase like garnet (Degeling et al., 2001; Figure 15) or högbomite, during which Zr was released and the lower Zr solubility in the newly formed retrograde phase precluded its uptake (e.g., chlorite; Degeling et al., 2001; Fraser et al., 1997). This likely promoted direct precipitation of baddeleyite/zircon crystals along the progressive reaction front until garnet or högbomite was completely consumed possibly by metasomatic fluids (Figure 2m). The potential breakdown of garnet and högbomite is supported by the formation of different chlorite species (e.g., clinochlore and sheridianite). Large rounded chlorite lenses rimmed by rutile in Figure 2i may be also explained by the breakdown of large garnet crystals.

5.2 | The role of mineral assemblage and fluids in the origin and transformation of baddeleyite to zircon

5.2.1 | Metamorphic or metasomatic baddeleyite?

Although most of the formation mechanisms for secondary baddeleyite have been usually attributed to subsolidus Zr diffusion from different parental phases (Bingen et al., 2001; Morisset & Scoates, 2008; Pape et al., 2016), other mechanisms have been reported from experiments. These mechanisms are usually associated with zircon alteration in the presence of Ca-, H_2O-, NaOH- and Na_2CO_3-bearing fluids (Ayers et al., 2012; Lewerentz et al., 2019; Rizvanova et al., 2000). Lewerentz et al. (2019) showed that partial fluid-mediated alteration of zircon to baddeleyite could be a function of both Ca and Si activities during amphibolite and granulite facies conditions. In their study, they show that baddeleyite "relicts" in zircon interiors are not always evidence of precursor baddeleyite reacting into zircon but instead the opposite. Zircon reacting to baddeleyite occurs according to the experiments when significant amounts of available Ca are present in the system, promoting the decrease of the SiO_2 activity below 1 in the fluid. As a consequence, baddeleyite becomes the stable phase (Lewerentz et al., 2019). Although we cannot discard this scenario for some baddeleyite formation in the RBI, several lines of evidence suggest that at least the majority of baddeleyite-zircon textures reflect the transformation of baddeleyite into zircon. Firstly, the interaction of Ca-rich fluids with zircon and the formation of secondary baddeleyite involves precipitation of a Ca-silicate (e.g., wollastonite [$CaSiO_3$]; Lewerentz et al., 2019). Despite careful examination of the minerals within and in the surroundings of the baddeleyite-zircon domains in the RBI, no signs of Ca-silicates were found including wollastonite or titanite, the latter occurring only in contacts with plagioclase lenses in other areas of the rock. However, if Ca was released into the fluid during albitization and sericitization of plagioclase in the RBI-hosting anorthosite and transported into the RBI through grain boundary circulation, it would be expected that zircon in the anorthosite would have also been exposed and partly transformed into baddeleyite, yet this is not observed (Figure 8b). Moreover, metamictization seems to be a critical factor to increase the reactivity of the zircon by Ca-rich fluids as metamict zircon is more prone to react than others (Lewerentz et al., 2019). Zircon crystals from the RBI are extremely depleted in U (median values 0.1–0.9 ppm) which strongly minimizes the potential effects of metamictization in their crystal lattice and thus subsequent alteration.

5.2.2 | Interaction of contrasting fluid compositions in anorthosite and RBI

In contrast to the RBI, associated silicate-rich rocks (anorthosite and OARA) preserve no evidence of pristine baddeleyite or baddeleyite relicts within zircon spatially associated with Ti-Fe oxides. The abundant presence of baddeleyite in the RBI and total absence of it in the anorthosite call for significant differences in the local conditions after the exsolution of baddeleyite (e.g., silica availability; Davidson & Van Breemen, 1988; Morisset & Scoates, 2008; Scoates & Chamberlain, 1995). Rheological differences between the plagioclase-rich anorthosite matrix (brittle) versus the ilmenite-rich RBI (plastic) may have played an important role in the amount of fluid circulating through their matrix (Putnis & Austrheim, 2010) and, therefore, in the subsequent formation of zircon by fluid-induced reactions. Ilmenite can accommodate significant deformation at high temperatures (Agar & Lloyd, 1997; Duchesne, 1999), likely hindering the extensive development of fluid circulation pathways besides those of grain boundaries. On the contrary, plagioclase fracturing is common during high-strain deformation (Rosenberg & Stünitz, 2003), potentially creating a denser network of fluid pathways in the anorthosite matrix and thus enhancing the interaction of baddeleyite with Si-rich fluids. Further evidence of higher Si-activity in the silicate-rich matrix is indicated by frequent titanite formation around rutile and ilmenite in the anorthosite (Figure 2c) and OARA, whereas titanite is extremely rare in the RBI.

The contrasting differences in CL patterns, trace-elements signatures and oxygen isotopic compositions between zircon from the RBI and the anorthosite (Figure 9; Weber et al., 2020) are likely evidence of distinct interaction and composition of fluids with baddeleyite/zircon during metamorphic growth. The chondrite-normalized REE patterns of Ediacaran and Ordovician metamorphic zircon from the anorthosite (Weber et al., 2020) show contrasting REE patterns to zircon from the RBI (Figure 9a–d). This chemical mismatch is also reflected in the $\delta^{18}O$ values of zircon crystals, which are distinguishable between the anorthosite ($\delta^{18}O = 4.9$–6.7‰) and the RBI zircon (5.0–10.2‰; Figure 9e–f). The $\delta^{18}O$ values for zircon in the RBI (Figure 9e) and trace elements (Figure S4) are inconsistent with the involvement of hydrothermal fluids during zircon growth, as this usually overprints an oxygen isotope composition to lower values relative to the zircon mantle value of ~5.3‰. Heterogenous oxygen isotope compositions between chemically distinct classes of zircon suggest that fluid-rock equilibration for oxygen isotopes was only achieved locally (closed system; Rubatto, 2017), or distinct fluids compositions were associated with each metamorphic event (open system).

The compositional contrast between the zircon population in the anorthosite and the RBI is further observed in the zircon U contents, which vary by almost three orders of magnitude between zircon of c. 620 and 450 Ma from the anorthosite (average ~530 ppm) and RBI (average ~1 ppm; Figure 10a). Morisset and Scoates (2008) suggested that low-U zircon genetically associated with ilmenite likely reflects inheritance from U-poor ilmenite (ilmenite-melt $D^{U}_{Ilm} < 10^{-4}$; Blundy & Wood, 2003). This could explain the extreme U depletion in zircon from the RBI. However, the much higher U abundances in zircon from the anorthosite and OARA indicate growth from fluids with higher U contents. Thus, we suggest that the RBI may have behaved as a closed system in which zircon formed from fluids that equilibrated only with the surrounding low-U minerals. By contrast, zircon from the anorthosite may have involved fluids equilibrating with minerals bearing higher U contents like primary clinopyroxene ($D^{U}_{Cpx} = 0.0049$–0.034; Blundy & Wood, 2003). Although for CMC anorthosites and related rocks the presence of clinopyroxene has not been reported, the presence of amphibole has been suggested to represent retrogression of primary mafic "dry" minerals like ortho- or clinopyroxene (Cisneros de León et al., 2017). Given that the RBI was presumably impervious to external fluids, it is likely that both REE and $\delta^{18}O$ compositions resulted from element redistribution and isotopic fractionation at a local scale during the breakdown and recrystallization/neo-crystallization of minerals (e.g., ilmenite, spinel, högbomite and chlorite) at each zircon-forming stage.

Further evidence of fluid heterogeneity between the comagmatic rocks may come from zircon Eu signatures. Zircon growing in equilibrium with feldspar is expected to show a negative Eu anomaly from the preferential uptake of Eu by plagioclase (Burnham et al., 2015; Rubatto, 2002). However, the incorporation of Eu into zircon may depend on the redox conditions at the time of zircon growth (Loader et al., 2017; Trail et al., 2012). The incorporation of Ce into zircon is also redox-sensitive, and the magnitude of the anomaly varies as a function of fO_2, such that ideally, zircon crystalizing in more oxidized systems have larger positive anomalies and smaller negative Eu anomalies (Loader et al., 2017; Trail et al., 2012). Ediacaran metamorphic zircon from anorthosite (Weber et al., 2020) is characterized by moderate to strong negative Eu anomalies (0.14–0.91: Figure 10d), whereas Ordovician zircon is characterized by moderate to strong positive Eu anomalies (1.39–17.2; Figure 10d). Zircon composition from the RBI falls mostly within

these two contrasting chemical signatures from anorthosite zircon, with compositions fluctuating near and on both sides of Eu/Eu* = 1 (Figure 10d). A negative correlation when plotting Eu/Eu* against Ce/Ce* from zircon of both the RBI and anorthosite (Figure 10d) is however in conflict with oxidation controlling the incorporation of Eu into zircon, but rather, we suggest that it indicates an influence of plagioclase abundance and fractionation. Thus, we consider that zircon from the RBI with slightly negative to positive Eu anomalies exchanged Eu with feldspar during crystallization or that feldspar was not abundant enough to have an impact on the Eu content in zircon (Figure 10d).

5.3 | Implications of the evolution of anorthosites in CMC

Zircon dates from anorthosite and comagmatic rocks studied in this work and those previously published (e.g., Cisneros de León et al., 2017; Estrada-Carmona et al., 2012; Weber et al., 2020), suggest several discrete zircon crystallization episodes associated with different thermal events (Figure 14). The age for anorthosite intrusion is well-constrained for Mexican exposures in Oaxaca, central and northern Mexico (c. 1010–1020 Ma; Keppie et al., 2003; Ortega-Gutiérrez et al., 2018); however, for the CMC anorthosite, the oldest zircon population—if ever present—has been mostly obliterated by the cumulative effects of several subsequent metamorphic episodes. Despite this limitation, few zircon crystals indicate incomplete resetting of their U–Pb system and suggest an age of c. 1.01 Ga (Estrada-Carmona et al., 2012). Intriguingly, the characteristic c. 990 Ma granulite facies metamorphism commonly evident in Oaxaquia (Solari et al., 2003) is either absent or younger in the CMC anorthosite zircon record (e.g., c. 950 Ma). Interestingly, an age cluster around younger Tonian ages with a weighted average mean age of 953 $^{+54}/_{-23}$ Ma (Figure 14) coincides within error with Tonian c. 950 Ma and c. 920 Ma metamorphic ages found in the Candelaria/Catarina and Chipilín units, respectively (Valencia-Morales et al., 2022; Weber et al., 2020). The metamorphic zircon ages around c. 920 Ma have been previously interpreted as resulting from the reactivation of a tectonic border through post-collisional extensional detachment faults (Weber et al., 2020), similar to the Dalane phase of metamorphism from the Sveconorwegian orogen of western Baltica (Bogdanova et al., 2008).

The minimum temperature estimate (~730°C) for the coarse-grained rutile (cores) in the RBI is within the range of rutile temperatures from Oaxaquia granulite facies rocks (c. 990 Ma) associated with the assembly of Rodinia (658–938°C; Adame-Martínez et al., 2020). The observed coarse-grained rutile temperature range in RBI rocks is higher than the temperature estimates reported for the c. 450 Ma metamorphic event in the southeastern CMC (El Triunfo Complex ~650°C; González-Guzmán et al., 2016; Weber et al., 2018). The range of zircon temperatures (545–797°C) shows on average slightly lower temperatures relative to the coarse-grained rutile, but some zircon grains overlap in the high-temperature range (>700°C). Current zircon crystallization temperatures for contact metamorphism associated with intrusion of rift-related mafic dyke swarm into the anorthosite at c. 620 Ma (associated with the Rodinia breakup and opening of the Iapetus Ocean; Weber et al., 2020) suggest a range from 605 to 740°C, with an average of 690°C. However, we discard this thermal event for the formation of coarse-grained rutile, as rutile occurrence is not restricted to metamorphic contact aureoles. Thus, the formation of rutile is attributed to the c. 950 Ma metamorphic event, which could be correlated to or post-dating the granulite facies metamorphism in Oaxaquia rocks which also extensively formed rutile (Solari et al., 2004).

Previous zircon LA-ICP-MS dating from the same RBI sample (ACL-5-10B; Cisneros de León et al., 2017) indicate ages of c. 550–600, c. 450 and c. 250 Ma that correlate to reported local and regional metamorphism (González-Guzmán et al., 2016; Weber et al., 2007, 2018, 2020). Similar age clusters are found in the hosting anorthosite (CH17-1; Figure 14). The largest population of zircon in the hosting anorthosite of 253 $^{+4}/_{-5}$ Ma (Figure 9a) agrees with a discordia line to 256 ± 7 Ma from the RBI (Figure 9b). This suggests that most zircon crystals underwent extensive recrystallization at this time, thus obliterating most of the previous record. The evidence of relatively large baddeleyite crystals conforming to a discordia date of 232 ± 15 Ma coupled to incipient or no transformation into zircon likely represents the youngest baddeleyite exsolution event (from ilmenite) and may be marginally post-dating the c. 250 Ma metamorphic event.

Minor peaks in the probability density function at 350–400 and 700–800 Ma occur mainly in the OARA. Zircons from OARA show evidence for compositional resetting in deformed intragrain zones identified by sharp CL intensity contrasts that are interpreted as annealed fractures (Figure 7a–d); *in situ* dating over domains with and without deformation shows contrasting U–Pb results, in which analysis spots placed over deformed zones yielded significantly younger dates (e.g., 456 ± 16 Ma vs 356 ± 10 Ma). This is likely due to deformation-driven partial Pb-loss (e.g., Kovaleva et al., 2017; Reddy et al., 2009) during Miocene shear events (Tonalá shear

zone; Molina-Garza et al., 2015). Therefore, such peaks in the age distribution may lack any geological significance.

Three zircon crystals from the Mariscal anorthosite (CH17-1) yielded concordant dates of c. 100–88 Ma. Remarkably, the older dates are identical within error to the 100 ± 11 Ma isochron age obtained from coarse-grained rutile from the RBI (Figure 13e). While Cretaceous metamorphism has been reported for the eastern segment of the Polochic-Motagua fault system, the data presented here are potentially the first record of this event in the western segment. The closest locality with a similar Cretaceous age is therefore ~200 km to the east along the Polochic Fault within the high-pressure metamorphic Chuacús Complex of Guatemala (see Figure 1b; Maldonado, Weber, et al., 2018; Martens et al., 2012; Ratschbacher et al., 2009). The timing of eclogite facies metamorphism in the Chuacús Complex has been dated with the Lu-Hf method on garnet and whole-rock aliquots from eclogite at 101 ± 3 and 95 ± 2 Ma, whereas zircon, monazite and titanite U–Pb ages indicate later-stage events at c. 80–74 Ma (Maldonado, Weber, et al., 2018). Zircon dating of meta-granitoids associated with eclogites showed protolith ages of c. 1.1–1.0 Ga and c. 224 Ma (Maldonado, Ortega-Gutiérrez et al., 2018; Solari et al., 2011). Tectonic reconstructions for the Cretaceous period suggest proximity between the southern CMC and the Chuacús Complex during the evolution of the Caribbean region, as both comprised the southern portion of the Maya Block (Maldonado, Ortega-Gutiérrez, et al., 2018; Maldonado, Weber, et al., 2018; Martens et al., 2017). We argue that our new geochronological evidence from rutile and zircon may reflect the timing of a high-pressure and relatively low-temperature tectonothermal disruption, which may be supported by the occurrence of phengitic mica in the anorthosites (Si [apfu] = 3.26 to 3.33; see Dataset S1). However, the tentative correlation of this event with the formation of the Chuacús metamorphic complex needs further investigation, which is beyond the scope of this paper.

At the western anorthosite exposure (Soconusco), rutile rims around ilmenite grains (Figure 2d,e; ENFORT-01) are reset to a near-zero age (7 ± 45 Ma), whereas OARA zircon from a nearby locality show ages as young as c. 3–4 Ma. Both anorthosite and OARA from this area were massively intruded by syntectonic granite plutons at c. 10 Ma (Molina-Garza et al., 2015). Whereas resetting of the rutile U–Pb system may be related to this event, the young zircon crystals from OARA are most likely related to resetting by Late Miocene ductile deformation (e.g., Piazolo et al., 2012).

6 | CONCLUSIONS

Massif-type anorthosite and Ti-Fe oxide-rich comagmatic rocks within the CMC in southeastern Mexico display a wide spectrum of zircon textures spatially associated with Zr-bearing igneous and metamorphic minerals. The complexity of CMC zircon textures is mirrored by heterogeneous U–Pb zircon ages in the hosting anorthosite and comagmatic rocks, revealing crystallization during a billion-year history that was punctuated by multiple metamorphic events. Textural relationships indicate that baddeleyite was the primordial mineral formed after Zr exsolution from igneous ilmenite and högbomite as well as from metamorphic rutile, ilmenite, högbomite, and garnet during slow cooling or mineral breakdown. While baddeleyite likely crystallized during cooling after individual igneous and metamorphic thermal pulses, zircon formed after baddeleyite in reactions during subsequent metamorphic events upon remobilization and redistribution of silica in fluids. The occurrence of non-igneous baddeleyite in mafic rocks and the evidence of Zr remobilization from rutile urges caution when interpreting age and thermometry results, especially if lacking any textural context.

ACKNOWLEDGEMENTS

We would like to thank Dr. Hans-Peter Meyer and Johannes Grimm (electron microprobe analysis and data reduction), Dr. Alexander Varychev (secondary electron microscopy) and Ilona Fin and Oliver Wienand (thin section preparation), all from Heidelberg Universität. Renée González Guzmán (CICESE) is thanked for zircon separation from anorthosite sample CH17-1. This paper was supported by DFG (Deutsche Forschungsgemeinschaft) grant SCHM 2521/4-1 and CONACYT (Consejo Nacional de Ciencia y Tecnología) CB-2016-01-285638. We thank Dr. Lorraine Tual and Dr. Renaud Soucy La Roche for their constructive comments. Editor Dr. Clare Warren is acknowledged for the editorial handling of the manuscript. Open Access funding enabled and organized by Projekt DEAL.

CONFLICT OF INTEREST

No conflict of interest to declare.

DATA AVAILABILITY STATEMENT

The data that support the findings of this study are available in the supporting information of this article.

ORCID

Alejandro Cisneros de León https://orcid.org/0000-0002-0133-2838
Axel K. Schmitt https://orcid.org/0000-0002-9029-4211
Bodo Weber https://orcid.org/0000-0002-5029-6087

REFERENCES

Adame-Martínez, M. G., Solari, L. A., Ortega-Obregón, C., & Abdullin, F. (2020). U-Pb geochronology of rutile: Deciphering the cooling history of the Oaxacan complex granulites, southern Mexico. *Revista Mexicana de Ciencias Geológicas*, *37*(2), 135–145. https://doi.org/10.22201/cgeo.20072902e.2020.2.1557

Agar, S. M., & Lloyd, G. E. (1997). Deformation of Fe-Ti oxides in gabbroic shear zones from the Mark area, *in* Proceedings-ocean Drilling Program Scientific Results1997, National Science Foundation, 123–142.

Austrheim, H., Putnis, C. V., Engvik, A. K., & Putnis, A. (2008). Zircon coronas around Fe–Ti oxides: A physical reference frame for metamorphic and metasomatic reactions. *Contributions to Mineralogy and Petrology*, *156*(4), 517–527. https://doi.org/10.1007/s00410-008-0299-8

Authemayou, C., Brocard, G., Teyssier, C., Simon-Labric, T., Guttiérrez, A., Chiquín, E., & Morán, S. (2011). The Caribbean–North America–Cocos Triple Junction and the dynamics of the Polochic–Motagua fault systems: Pull-up and zipper models. *Tectonics*, *30*(3), TC3010. https://doi.org/10.1029/2010TC002814

Ayers, J. C., Zhang, L., Luo, Y., & Peters, T. (2012). Zircon solubility in alkaline aqueous fluids at upper crustal conditions. *Geochimica et Cosmochimica Acta*, *96*, 18–28. https://doi.org/10.1016/j.gca.2012.08.027

Bea, F., Montero, P., & Ortega, M. (2006). A LA–ICP–MS evaluation of Zr reservoirs in common crustal rocks: Implications for Zr and Hf geochemistry, and zircon-forming processes. *The Canadian Mineralogist*, *44*(3), 693–714. https://doi.org/10.2113/gscanmin.44.3.693

Beckman, V., & Möller, C. (2018). Prograde metamorphic zircon formation in gabbroic rocks: The tale of microtextures. *Journal of Metamorphic Geology*, *36*(9), 1221–1236. https://doi.org/10.1111/jmg.12443

Beckman, V., Möller, C., Söderlund, U., & Andersson, J. (2017). Zircon growth during progressive recrystallization of gabbro to garnet amphibolite, Eastern Segment, Sveconorwegian Orogen. *Journal of Petrology*, *58*(1), 167–187. https://doi.org/10.1093/petrology/egx009

Beckman, V., Möller, C., Söderlund, U., Corfu, F., Pallon, J., & Chamberlain, K. R. (2014). Metamorphic zircon formation at the transition from gabbro to eclogite in Trollheimen–Surnadalen, Norwegian Caledonides. *Geological Society, London, Special Publications*, *390*(1), 403–424. https://doi.org/10.1144/SP390.26

Beura, D., Acharya, D., Singh, P., & Acharya, S. (2009). Högbomite associated with vanadium bearing titaniferous magnetite of mafic-ultramafic suite of Moulabhanj igneous complex, Orissa, India. *Journal of Minerals and Materials Characterization and Engineering*, *8*(09), 745–753. https://doi.org/10.4236/jmmce.2009.89064

Bingen, B., Austrheim, H., & Whitehouse, M. (2001). Ilmenite as a source for zirconium during high-grade metamorphism? Textural Evidence from the Caledonides of Western Norway and Implications for Zircon Geochronology. *Journal of Petrology*, *42*(2), 355–375. https://doi.org/10.1093/petrology/42.2.355

Blackburn, T., Shimizu, N., Bowring, S. A., Schoene, B., & Mahan, K. H. (2012). Zirconium in rutile speedometry: New constraints on lower crustal cooling rates and residence temperatures. *Earth and Planetary Science Letters*, *317–318*, 231–240.

Blundy, J., & Wood, B. (2003). Mineral-melt partitioning of uranium, thorium and their daughters. *Reviews in Mineralogy and Geochemistry*, *52*(1), 59–123. https://doi.org/10.2113/0520059

Bogdanova, S., Bingen, B., Gorbatschev, R., Kheraskova, T., Kozlov, V., Puchkov, V., & Volozh, Y. A. (2008). The east European craton (Baltica) before and during the assembly of Rodinia. *Precambrian Research*, *160*(1–2), 23–45. https://doi.org/10.1016/j.precamres.2007.04.024

Booth, A. L., Kolodny, Y., Chamberlain, C. P., McWilliams, M., Schmitt, A. K., & Wooden, J. (2005). Oxygen isotopic composition and U-Pb discordance in zircon. *Geochimica et Cosmochimica Acta*, *69*(20), 4895–4905. https://doi.org/10.1016/j.gca.2005.05.013

Briggs, R. A., & Sacco, A. (1993). The oxidation of llmenite and its relationship to the FeO-Fe_2O_3-TiO_2 phase diagram at 1073 and 1140 K. *Metallurgical and Materials Transactions A*, *24*(6), 1257–1264. https://doi.org/10.1007/BF02668194

Burnham, A. D., Berry, A. J., Halse, H. R., Schofield, P. F., Cibin, G., & Mosselmans, J. F. W. (2015). The oxidation state of europium in silicate melts as a function of oxygen fugacity, composition and temperature. *Chemical Geology*, *411*, 248–259. https://doi.org/10.1016/j.chemgeo.2015.07.002

Charlier, B., Skår, Ø., Korneliussen, A., Duchesne, J.-C., & Vander Auwera, J. (2007). Ilmenite composition in the Tellnes Fe–Ti deposit, SW Norway: Fractional crystallization, postcumulus evolution and ilmenite–zircon relation. *Contributions to Mineralogy and Petrology*, *154*(2), 119–134. https://doi.org/10.1007/s00410-007-0186-8

Cherniak, D., Manchester, J., & Watson, E. (2007). Zr and Hf diffusion in rutile. *Earth and Planetary Science Letters*, *261*(1), 267–279. https://doi.org/10.1016/j.epsl.2007.06.027

Cisneros de León, A., Weber, B., Ortega-Gutiérrez, F., González-Guzmán, R., Maldonado, R., Solari, L., Schaaf, P., & Manjarrez-Juárez, R. (2017). Grenvillian massif-type anorthosite suite in Chiapas, Mexico: Magmatic to polymetamorphic evolution of anorthosites and their Ti-Fe ores. *Precambrian Research*, *295*, 203–226. https://doi.org/10.1016/j.precamres.2017.04.028

Coombs, H., Kerr, A., Pindell, J., Buchs, D., Weber, B., & Solari, L. (2020). Petrogenesis of the Crystalline Basement along the Western Gulf of Mexico: Post-Collisional Magmatism during the Formation of Pangea: Geological Society of America Special Papers, *546*.

Davidson, A., & Van Breemen, O. (1988). Baddeleyite-zircon relationships in coronitic metagabbro, Grenville Province, Ontario: Implications for geochronology. *Contributions to Mineralogy and Petrology*, *100*(3), 291–299. https://doi.org/10.1007/BF00379740

Degeling, H., Eggins, S., & Ellis, D. (2001). Zr budgets for metamorphic reactions, and the formation of zircon from garnet breakdown. *Mineralogical Magazine*, *65*(6), 749–758. https://doi.org/10.1180/0026461016560006

Devaraju, T., Jayaraj, K., Sudhakara, T., Alapieti, T., Spiering, B., & Kaukonen, R. (2014). Mineralogy, geochemistry and petrogenesis of the V-Ti-bearing and chromiferous magnetite deposits hosted by Neoarchaean Channagiri mafic-ultramafic complex, Western Dharwar Craton, India: Implications for

Emplacement in Differentiated Pulses. *Open Geosciences*, *6*(4), 518–548. https://doi.org/10.2478/s13533-012-0193-9

Devaraju, T., Uttangi, V., & Coolen, J. (1981). Hogbomite from Fe-Ti deposits of Madangere, Ankola Taluk, Karnataka. *Geological Society of India*, *22*(9), 439–443.

Duchesne, J. C. (1999). Fe-Ti deposits in Rogaland anorthosites (South Norway): Geochemical characteristics and problems of interpretation. *Mineralium Deposita*, *34*(2), 182–198. https://doi.org/10.1007/s001260050195

Estrada-Carmona, J., Weber, B., Martens, U., & López-Martínez, M. (2012). Petrogenesis of Ordovician magmatic rocks in the southern Chiapas massif complex: Relations with the early Palaeozoic magmatic belts of northwestern Gondwana. *International Geology Review*, *54*(16), 1918–1943. https://doi.org/10.1080/00206814.2012.685553

Ewing, T. A., Hermann, J., & Rubatto, D. (2013). The robustness of the Zr-in-rutile and Ti-in-zircon thermometers during high-temperature metamorphism (Ivrea-Verbano zone, northern Italy). *Contributions to Mineralogy and Petrology*, *165*(4), 757–779. https://doi.org/10.1007/s00410-012-0834-5

Ferry, J. M., & Watson, E. B. (2007). New thermodynamic models and revised calibrations for the Ti-in-zircon and Zr-in-rutile thermometers. *Contributions to Mineralogy and Petrology*, *154*(4), 429–437. https://doi.org/10.1007/s00410-007-0201-0

Fraser, G., Ellis, D., & Eggins, S. (1997). Zirconium abundance in granulite-facies minerals, with implications for zircon geochronology in high-grade rocks. *Geology*, *25*(7), 607–610. https://doi.org/10.1130/0091-7613(1997)025<0607:ZAIGFM>2.3.CO;2

French, C. D., & Schenk, C. J. (2006). Map showing geology, oil and gas fields, and geologic provinces of the Gulf of Mexico Region, 2331-1258.

González-Guzmán, R., Weber, B., Manjarrez-Juárez, R., Cisneros de León, A., Hecht, L., & Herguera-García, J. C. (2016). Provenance, age constraints and metamorphism of Ediacaran metasedimentary rocks from the El Triunfo complex (SE Chiapas, México): Evidence for Rodinia breakup and Iapetus active margin. *International Geology Review*, *58*(16), 2065–2091. https://doi.org/10.1080/00206814.2016.1207208

Grew, E. S., Hiroi, Y., & Shiraishi, K. (1990). Högbomite from the Prince Olav coast, East Antarctica: An example of oxidation-exsolution of a complex magnetite solid solution? *American Mineralogist*, *75*, 589400.

Guzmán-Speziale, M., & Meneses-Rocha, J. J. (2000). The North America–Caribbean plate boundary west of the Motagua–Polochic fault system: a fault jog in Southeastern Mexico. *Journal of South American Earth Sciences*, *13*(4–5), 459–468. https://doi.org/10.1016/S0895-9811(00)00036-5

Harley, S. L., Kelly, N. M., & Möller, A. (2007). Zircon behaviour and the thermal histories of mountain chains. *Elements*, *3*(1), 25–30. https://doi.org/10.2113/gselements.3.1.25

Heaman, L., & LeCheminant, A. (1993). Paragenesis and U-Pb systematics of baddeleyite (ZrO2). *Chemical Geology*, *110*(1–3), 95–126. https://doi.org/10.1016/0009-2541(93)90249-I

Hoskin, P. W. (2005). Trace-element composition of hydrothermal zircon and the alteration of hadean zircon from the Jack Hills, Australia. *Geochimica et Cosmochimica Acta*, *69*(3), 637–648. https://doi.org/10.1016/j.gca.2004.07.006

Hoskin, P. W. O., & Black, L. P. (2000). Metamorphic zircon formation by solid-state recrystallization of protolith igneous zircon. *Journal of Metamorphic Geology*, *18*(4), 423–439. https://doi.org/10.1046/j.1525-1314.2000.00266.x

Jayaraj, K., Khanadali, S., Devaraju, T., & Spiering, B. (1995). A Study of Hogbomite in the V-Ti-Fe Deposits of Karnataka. *Geological Society of India*, *45*(1), 57–64.

Jiao, S., Guo, J., Mao, Q., & Zhao, R. (2011). Application of Zr-in-rutile thermometry: A case study from ultrahigh-temperature granulites of the Khondalite belt, North China Craton. *Contributions to Mineralogy and Petrology*, *162*(2), 379–393. https://doi.org/10.1007/s00410-010-0602-3

Keppie, J. D., Dostal, J., Cameron, K. L., Solari, L. A., Ortega-Gutiérrez, F., & Lopez, R. (2003). Geochronology and geochemistry of Grenvillian igneous suites in the northern Oaxacan complex, southern Mexico: Tectonic implications. *Precambrian Research*, *120*(3–4), 365–389. https://doi.org/10.1016/S0301-9268(02)00166-3

Kohn, M. J., Corrie, S. L., & Markley, C. (2015). The fall and rise of metamorphic zircon. *American Mineralogist*, *100*(4), 897–908. https://doi.org/10.2138/am-2015-5064

Konzett, J., Miller, C., Armstrong, R., & Thöni, M. (2005). Metamorphic Evolution of Iron-rich Mafic Cumulates from the Otztal-Stubai Crystalline Complex, Eastern Alps, Austria. *Journal of Petrology*, *46*(4), 717–747. https://doi.org/10.1093/petrology/egh095

Kooijman, E., Smit, M. A., Mezger, K., & Berndt, J. (2012). Trace element systematics in granulite facies rutile: Implications for Zr geothermometry and provenance studies. *Journal of Metamorphic Geology*, *30*(4), 397–412. https://doi.org/10.1111/j.1525-1314.2012.00972.x

Kovaleva, E., Klötzli, U., Habler, G., Huet, B., Guan, Y., & Rhede, D. (2017). The effect of crystal-plastic deformation on isotope and trace element distribution in zircon: Combined BSE, CL, EBSD, FEG-EMPA and NanoSIMS Study. *Chemical Geology*, *450*, 183–198.

Lawlor, P. J., Ortega-Gutiérrez, F., Cameron, K. L., Ochoa-Camarillo, H., Lopez, R., & Sampson, D. E. (1999). U–Pb geochronology, geochemistry, and provenance of the Grenvillian Huiznopala Gneiss of Eastern Mexico. *Precambrian Research*, *94*(1–2), 73–99. https://doi.org/10.1016/S0301-9268(98)00108-9

Lewerentz, A., Harlov, D. E., Scherstén, A., & Whitehouse, M. J. (2019). Baddeleyite formation in zircon by Ca-bearing fluids in silica-saturated systems in nature and experiment: resetting of the U–Pb geochronometer. *Contributions to Mineralogy and Petrology*, *174*(8), 1–25.

Liati, A., & Seidel, E. (1994). Sapphirine and högbomite in overprinted kyanite-eclogites of central Rhodope, N. Greece: First evidence of granulite-facies metamorphism. *European Journal of Mineralogy*, *6*(5), 733–737. https://doi.org/10.1127/ejm/6/5/0733

Loader, M. A., Wilkinson, J. J., & Armstrong, R. N. (2017). The effect of titanite crystallisation on Eu and Ce anomalies in zircon and its implications for the assessment of porphyry cu deposit fertility. *Earth and Planetary Science Letters*, *472*, 107–119.

Ludwig, K. (2003). *User's Manual for Isoplot 3.00: A Geochronological Toolkit for Microsoft Excel*. Berkeley geochronology center special Publication. no. 4

Luvizotto, G. L., & Zack, T. (2009). Nb and Zr behavior in rutile during high-grade metamorphism and retrogression: An example from the Ivrea–Verbano Zone. *Chemical Geology*, *261*(3–4), 303–317. https://doi.org/10.1016/j.chemgeo.2008.07.023

Luvizotto, G. L., Zack, T., Meyer, H. P., Ludwig, T., Triebold, S., Kronz, A., Münker, C., Stockli, D. F., Prowatke, S., Klemme, S., Jacob, D. E., & von Eynatten, H. (2009). Rutile crystals as potential trace element and isotope mineral standards for microanalysis. *Chemical Geology*, *261*(3–4), 346–369. https://doi.org/10.1016/j.chemgeo.2008.04.012

Maldonado, R., Ortega-Gutiérrez, F., & Ortíz-Joya, G. A. (2018). Subduction of Proterozoic to late Triassic continental basement in the Guatemala suture zone: A petrological and geochronological study of high-pressure metagranitoids from the Chuacús complex. *Lithos*, *308*, 83–103.

Maldonado, R., Weber, B., Ortega-Gutiérrez, F., & Solari, L. A. (2018). High-pressure metamorphic evolution of eclogite and associated metapelite from the Chuacús complex (Guatemala suture zone): Constraints from phase equilibria modelling coupled with Lu-Hf and U-Pb geochronology. *Journal of Metamorphic Geology*, *36*(1), 95–124. https://doi.org/10.1111/jmg.12285

Mancktelow, N. (1981). Högbomite of unusual composition from Reedy Creek, South Australia. *Mineralogical Magazine*, *44*(333), 91–94.

Martens, U., Tsujimori, T., & Liou, J. G. (2017). Eclogite varieties and petrotectonic evolution of the northern Guatemala suture complex. *International Geology Review*, *59*(5–6), 721–740. https://doi.org/10.1080/00206814.2016.1245592

Martens, U. C., Brueckner, H. K., Mattinson, C. G., Liou, J. G., & Wooden, J. L. (2012). Timing of eclogite-facies metamorphism of the Chuacús complex, Central Guatemala: Record of late cretaceous continental subduction of North America's sialic basement. *Lithos*, *146–147*, 1–10.

Meyer, M., John, T., Brandt, S., & Klemd, R. (2011). Trace element composition of rutile and the application of Zr-in-rutile thermometry to UHT metamorphism (Epupa complex, NW Namibia). *Lithos*, *126*(3–4), 388–401. https://doi.org/10.1016/j.lithos.2011.07.013

Mohanty, J., Sahoo, R., & Paul, A. (1995). Research note on Högbomite from Fe-Ti oxide deposit, Boula-Nausahi Igneous Complex. *Ind. Miner*, *49*(4), 293–294.

Molina-Garza, R. S., Geissman, J. W., Wawrzyniec, T. F., Alonso, T. A. P., Iriondo, A., Weber, B., & Aranda-Gómez, J. (2015). Geology of the coastal Chiapas (Mexico) Miocene plutons and the Tonalá shear zone: Syntectonic emplacement and rapid exhumation during sinistral transpression. *Lithosphere*, *7*(3), 257–274. https://doi.org/10.1130/L409.1

Morishita, T., Maeda, J., Miyashita, S., Matsumoto, T., & Dick, H. J. (2004). Magmatic srilankite (Ti_2ZrO_6) in gabbroic vein cutting oceanic peridotites: An unusual product of peridotite-melt interactions beneath slow-spreading ridges. *American Mineralogist*, *89*(5–6), 759–766. https://doi.org/10.2138/am-2004-5-609

Morisset, C.-E., & Scoates, J. S. (2008). Origin of zircon rims around ilmenite in mafic plutonic rocks of Proterozoic anorthosite suites. *The Canadian Mineralogist*, *46*(2), 289–304. https://doi.org/10.3749/canmin.46.2.289

Naslund, H. R. (1987). Lamellae of baddeleyite and Fe-Cr-spinel in ilmenite from the Basistoppen sill, East Greenland. *The Canadian Mineralogist*, *25*(1), 91–96.

Nishimiya, Y., Tsunogae, T., Santosh, M., Dubessy, J., & Chetty, T. (2009). Prograde and retrograde högbomites in sapphirine+quartz bearing mg-Al rock from the Palghat-Cauvery suture zone, southern India. *Journal of Mineralogical and Petrological Sciences*, *104*(5), 319–323. https://doi.org/10.2465/jmps.090613

Ortega-Gutiérrez, F., Elías-Herrera, M., Morán-Zenteno, D. J., Solari, L., Weber, B., & Luna-González, L. (2018). The pre-Mesozoic metamorphic basement of Mexico, 1.5 billion years of crustal evolution. *Earth-Science Reviews*, *183*, 2–37. https://doi.org/10.1016/j.earscirev.2018.03.006

Ortega-Gutiérrez, F., Mitre-Salazar, L., Roldan-Quintana, J., & de Recursos Minerales, C. (1992). Carta geológica de la República Mexicana, Consejo de Recursos Minerales y en el Instituto de Geología de la UNAM.

Ortega-Gutiérrez, F., Solari, L. A., Ortega-Obregón, C., Elías-Herrera, M., Martens, U., Morán-Icál, S., Chiquín, M., Keppie, J. D., De León, R. T., & Schaaf, P. (2007). The Maya-Chortís boundary: A tectonostratigraphic approach. *International Geology Review*, *49*(11), 996–1024. https://doi.org/10.2747/0020-6814.49.11.996

Pape, J., Mezger, K., & Robyr, M. (2016). A systematic evaluation of the Zr-in-rutile thermometer in ultra-high temperature (UHT) rocks. *Contributions to Mineralogy and Petrology*, *171*(5), 1–20.

Paulson, E. G. (1964). Mineralogy and origin of the titaniferous deposit at Pluma Hidalgo, Oaxaca, Mexico. *Economic Geology*, *59*(5), 753–767.

Perumala, R. V., & Merkle, R. K. (2014). Hydrothermal Högbomite associated with Vanadiferous-Titaniferous (V-Ti) bearing magnetite bands in Bhakatarhalli chromite mine, Nuggihalli Greenstone Belt, Western Dharwar Craton, Karnataka, India. *Acta Geologica Sinica (English Edition)*, *88*(3), 845–853. https://doi.org/10.1111/1755-6724.12241

Petersen, E., Essene, E. J., Peacor, D. R., & Marcotty, L. (1989). The occurrence of högbomite in high-grade metamorphic rocks. *Contributions to Mineralogy and Petrology*, *101*(3), 350–360. https://doi.org/10.1007/BF00375319

Piazolo, S., Austrheim, H., & Whitehouse, M. (2012). Brittle-ductile microfabrics in naturally deformed zircon: Deformation mechanisms and consequences for U-Pb dating. *American Mineralogist*, *97*(10), 1544–1563. https://doi.org/10.2138/am.2012.3966

Pouchou, J., & Pichoir, F. (1985). "PAP" φ (ρZ) procedure for improved quantitative microanalysis. In J. T. Armstrong (Ed.), *Microbeam Analysis* (pp. 104–106). San Francisco Press.

Pujol-Solà, N., Proenza, J. A., Garcia-Casco, A., González-Jiménez, J. M., Román-Alpiste, M. J., Garrido, C. J., Melgarejo, J. C., Gervilla, F., & Llovet, X. (2020). Fe-Ti-Zr metasomatism in the oceanic mantle due to extreme differentiation of tholeiitic melts (moa-Baracoa ophiolite, Cuba). *Lithos*, *358-359*, 105420. https://doi.org/10.1016/j.lithos.2020.105420

Putnis, A., & Austrheim, H. (2010). Fluid-Induced Processes: Metasomatism and Metamorphism. *Geofluids*, *10*(1–2), 254–269.

Rakotonandrasana, N. O. T., Arima, M., Miyawaki, R., & Rambeloson, R. A. (2010). Widespread occurrences of Högbomite-2*N*2*S* in UHT Metapelites from the Betroka Belt, southern Madagascar: Implications on melt or fluid activity during

regional metamorphism. *Journal of Petrology*, *51*, 869–895. https://doi.org/10.1093/petrology/egq004

Ratschbacher, L., Franz, L., Min, M., Bachmann, R., Martens, U., Stanek, K., Stübner, K., Nelson, B. K., Herrmann, U., & Weber, B. (2009). The north American-Caribbean plate boundary in Mexico-Guatemala-Honduras. *Geological Society, London, Special Publications*, *328*(1), 219–293. https://doi.org/10.1144/SP328.11

Razakamanana, T., Ackermand, D., & Windley, B. (2000). Högbomite in migmatitic paragneiss in the Betroka shear belt, Vohidava area, Precambrian of southern Madagascar. *Mineralogy and Petrology*, *68*(4), 257–269. https://doi.org/10.1007/s007100050012

Reddy, S. M., Timms, N. E., Hamilton, P. J., & Smyth, H. R. (2009). Deformation-related microstructures in magmatic zircon and implications for diffusion. *Contributions to Mineralogy and Petrology*, *157*(2), 231–244. https://doi.org/10.1007/s00410-008-0331-z

Rizvanova, N., Levchenkov, O., Belous, A., Bezmen, N., Maslenikov, A., Komarov, A., Makeev, A., & Levskiy, L. (2000). Zircon reaction and stability of the U-Pb isotope system during interaction with carbonate fluid: Experimental hydrothermal study. *Contributions to Mineralogy and Petrology*, *139*(1), 101–114. https://doi.org/10.1007/s004100050576

Rosenberg, C. L., & Stünitz, H. (2003). Deformation and recrystallization of plagioclase along a temperature gradient: An example from the Bergell tonalite. *Journal of Structural Geology*, *25*(3), 389–408. https://doi.org/10.1016/S0191-8141(02)00036-6

Rubatto, D. (2002). Zircon trace element geochemistry: partitioning with garnet and the link between U–Pb ages and metamorphism. *Chemical Geology*, *184*(1–2), 123–138. https://doi.org/10.1016/S0009-2541(01)00355-2

Rubatto, D. (2017). Zircon: The metamorphic mineral. *Reviews in Mineralogy and Geochemistry*, *83*(1), 261–295. https://doi.org/10.2138/rmg.2017.83.9

Schaaf, P., Weber, B., Weis, P., Groß, A., Ortega-Gutiérrez, F., & Köhler, H. (2002). The Chiapas massif (Mexico) revised: New geologic and isotopic data and basement characteristics. *Neues Jahrbuch fur Geologie Und Palaontologie - Abhandlungen*, *225*(1), 1–23. https://doi.org/10.1127/njgpa/225/2002/1

Schmitt, A. K., Chamberlain, K. R., Swapp, S. M., & Harrison, T. M. (2010). In situ U–Pb dating of micro-baddeleyite by secondary ion mass spectrometry. *Chemical Geology*, *269*(3), 386–395. https://doi.org/10.1016/j.chemgeo.2009.10.013

Schmitt, A. K., & Zack, T. (2012). High-sensitivity U–Pb rutile dating by secondary ion mass spectrometry (SIMS) with an O_2^+ primary beam. *Chemical Geology*, *332–333*, 65–73.

Schmitz, M. D., Bowring, S. A., & Ireland, T. R. (2003). Evaluation of Duluth complex anorthositic series (AS3) zircon AS a U-Pb geochronological standard: New high-precision isotope dilution thermal ionization mass spectrometry results. *Geochimica et Cosmochimica Acta*, *67*(19), 3665–3672. https://doi.org/10.1016/S0016-7037(03)00200-X

Scoates, J. S., & Chamberlain, K. R. (1995). Baddeleyite (ZrO_2) and zircon ($ZrSiO_4$) from anorthositic rocks of the Laramie anorthosite complex, Wyoming: Petrologic consequences and U-Pb ages. *American Mineralogist*, *80*(11), 1317–1327. https://doi.org/10.2138/am-1995-11-1222

Sengupta, P., Bhui, U. K., Braun, I., Dutta, U., & Mukhopadhyay, D. (2009). Chemical substitutions, paragenetic relations, and physical conditions of formation of högbomite in the Sittampundi layered anorthosite complex, South India. *American Mineralogist*, *94*(11–12), 1520–1534.

Shannon, R. (1976). In R. G. J. Strens (Ed.), *Systematic Studies of Interatomic Distances in Oxides: Physics and Chemistry of Minerals and Rocks* (pp. 403–431). John Wiley & Sons.

Sláma, J., Kosler, J., & Pedersen, R. B. (2007). Behaviour of zircon in high-grade metamorphic rocks: Evidence from Hf isotopes, trace elements and textural studies.: Contrib. *Mineralogy and Petrology*, *154*, 335–356. https://doi.org/10.1007/s00410-007-0196-6

Söderlund, P., Söderlund, U., Möller, C., Gorbatschev, R., & Rodhe, A. (2004). Petrology and ion microprobe U-Pb chronology applied to a metabasic intrusion in southern Sweden: A study on zircon formation during metamorphism and deformation. *Tectonics*, *23*(5), TC5005. https://doi.org/10.1029/2003TC001498

Söderlund, U., Hellström, F. A., & Kamo, S. L. (2008). Geochronology of high-pressure mafic granulite dykes in SW Sweden: tracking the P–T–t path of metamorphism using Hf isotopes in zircon and baddeleyite. *Journal of Metamorphic Geology*, *26*(5), 539–560. https://doi.org/10.1111/j.1525-1314.2008.00776.x

Solari, L. A., Keppie, J. D., López, R., Cameron, K. L., & Gutiérrez, F. O. (2004). ~ 990 ma peak granulitic metamorphism and amalgamation of Oaxaquia, Mexico: U-Pb zircon geochronological and common Pb isotopic data. *Revista Mexicana de Ciencias Geológicas*, *21*(2), 212–225.

Solari, L. A., Keppie, J. D., Ortega-Gutiérrez, F., Cameron, K. L., Lopez, R., & Hames, W. E. (2003). 990 and 1100 Ma Grenvillian tectonothermal events in the northern Oaxacan complex, southern Mexico: Roots of an orogen. *Tectonophysics*, *365*(1–4), 257–282. https://doi.org/10.1016/S0040-1951(03)00025-8

Solari, L. A., Tuena, A. G., Gutiérrez, F. O., & Obregón, C. O. (2011). The Chuacús metamorphic complex, Central Guatemala: Geochronological and geochemical constraints on its Paleozoic-Mesozoic evolution. *Geologica Acta*, *9*(3–4), 329–350.

Szymanowski, D., Fehr, M. A., Guillong, M., Coble, M. A., Wotzlaw, J.-F., Nasdala, L., Ellis, B. S., Bachmann, O., & Schönbächler, M. (2018). Isotope-dilution anchoring of zircon reference materials for accurate Ti-in-zircon thermometry. *Chemical Geology*, *481*, 146–154. https://doi.org/10.1016/j.chemgeo.2018.02.001

Taylor-Jones, K., & Powell, R. (2015). Interpreting zirconium-in-rutile thermometric results. *Journal of Metamorphic Geology*, *33*(2), 115–122. https://doi.org/10.1111/jmg.12109

Tomkins, H., Powell, R., & Ellis, D. (2007). The pressure dependence of the zirconium-in-rutile thermometer. *Journal of Metamorphic Geology*, *25*(6), 703–713. https://doi.org/10.1111/j.1525-1314.2007.00724.x

Trail, D., Bruce Watson, E., & Tailby, N. D. (2012). Ce and Eu anomalies in zircon as proxies for the oxidation state of magmas. *Geochimica et Cosmochimica Acta*, *97*, 70–87. https://doi.org/10.1016/j.gca.2012.08.032

Trail, D., Mojzsis, S. J., Harrison, T. M., Schmitt, A. K., Watson, E. B., & Young, E. D. (2007). Constraints on hadean

zircon protoliths from oxygen isotopes, Ti-thermometry, and rare earth elements. *Geochemistry, Geophysics, Geosystems*, *8* (6), Q06014. https://doi.org/10.1029/2006GC001449

Troitzsch, U., Christy, A., & Ellis, D. (2005). The Crystal Structure of Disordered (Zr,Ti)O_2 Solid Solution Including Srilankite: Evolution towards Tetragonal ZrO_2 with Increasing Zr. *Physics and Chemistry of Minerals*, *32*(7), 504–514. https://doi.org/10.1007/s00269-005-0027-0

Troitzsch, U., & Ellis, D. J. (2004). High-PT study of solid solutions in the system ZrO_2-TiO_2: The stability of srilankite. *European Journal of Mineralogy*, *16*(4), 577–584. https://doi.org/10.1127/0935-1221/2004/0016-0577

Troitzsch, U., & Ellis, D. J. (2005). The ZrO_2-TiO_2 phase diagram. *Journal of Materials Science*, *40*(17), 4571–4577. https://doi.org/10.1007/s10853-005-1116-7

Tual, L., Möller, C., & Whitehouse, M. (2018). Tracking the prograde P–T path of Precambrian eclogite using Ti-in-quartz and Zr-in-rutile geothermobarometry. *Contributions to Mineralogy and Petrology*, *173*(7), 1–15.

Valencia-Morales, Y. T., Weber, B., Tazzo-Rangel, M. D., González-Guzmán, R., Frei, D., Quintana-Delgado, J. A., & Rivera-Moreno, E. N. (2022). Early Mesoproterozoic inliers in the Chiapas massif complex of southern Mexico: Implications on Oaxaquia-Amazonia-Baltica configuration. *Precambrian Research*, *373*, 106611. https://doi.org/10.1016/j.precamres.2022.106611

Visser, D., Thijssen, P., & Schumacher, J. (1992). Högbomite in sapphirine-bearing rocks from the Bamble sector, South Norway. *Mineralogical Magazine*, *56*, 343–351. https://doi.org/10.1180/minmag.1992.056.384.06

Wang, L., Essene, E. J., & Zhang, Y. (1999). Mineral inclusions in pyrope crystals from garnet ridge, Arizona, USA: Implications for processes in the upper mantle. *Contributions to Mineralogy and Petrology*, *135*(2–3), 164–178. https://doi.org/10.1007/s004100050504

Weber, B., González-Guzmán, R., Manjarrez-Juárez, R., Cisneros de León, A., Martens, U., Solari, L., Hecht, L., & Valencia, V. A. (2018). Late Mesoproterozoic to early Paleozoic history of metamorphic basement from the southeastern Chiapas massif complex, Mexico, and Implications for the Evolution of NW Gondwana. *Lithos*, *300-301*, 177–199. https://doi.org/10.1016/j.lithos.2017.12.009

Weber, B., & Hecht, L. (2003). Petrology and geochemistry of metaigneous rocks from a Grenvillian basement fragment in the Maya block: The Guichicovi complex, Oaxaca, Southern Mexico. *Precambrian Research*, *124*(1), 41–67. https://doi.org/10.1016/S0301-9268(03)00078-0

Weber, B., Iriondo, A., Premo, W. R., Hecht, L., & Schaaf, P. (2007). New insights into the history and origin of the southern Maya block, SE México: U-Pb-SHRIMP Zircon Geochronology from Metamorphic Rocks of the Chiapas Massif. *International Journal of Earth Sciences*, *96*(2), 253–269. https://doi.org/10.1007/s00531-006-0093-7

Weber, B., Scherer, E. E., Schulze, C., Valencia, V. A., Montecinos, P., Mezger, K., & Ruiz, J. (2010). U–Pb and Lu–Hf isotope systematics of lower crust from central-southern Mexico – Geodynamic significance of Oaxaquia in a Rodinia Realm. *Precambrian Research*, *182*(1–2), 149–162. https://doi.org/10.1016/j.precamres.2010.07.007

Weber, B., Schmitt, A. K., Cisneros de León, A., González-Guzmán, R., & Gerdes, A. (2020). Neoproterozoic extension and the central Iapetus Magmatic Province in southern Mexico – New U-Pb ages, Hf-O Isotopes and Trace Element Data of Zircon from the Chiapas Massif Complex. *Gondwana Research*, *88*, 1–20. https://doi.org/10.1016/j.gr.2020.06.022

Whitney, D. L., & Evans, B. W. (2010). Abbreviations for names of rock-forming minerals. *American Mineralogist*, *95*(1), 185–187. https://doi.org/10.2138/am.2010.3371

Wiedenbeck, M., Hanchar, J. M., Peck, W. H., Sylvester, P., Valley, J., Whitehouse, M., Kronz, A., Morishita, Y., Nasdala, L., & Fiebig, J. (2004). Further characterisation of the 91500 zircon crystal. *Geostandards and Geoanalytical Research*, *28*(1), 9–39. https://doi.org/10.1111/j.1751-908X.2004.tb01041.x

Zack, T., Moraes, R., & Kronz, A. (2004). Temperature dependence of Zr in rutile: Empirical calibration of a rutile thermometer. *Contributions to Mineralogy and Petrology*, *148*(4), 471–488. https://doi.org/10.1007/s00410-004-0617-8

Zack, T., von Eynatten, H., & Kronz, A. (2004). Rutile geochemistry and its potential use in quantitative provenance studies. *Sedimentary Geology*, *171*(1–4), 37–58. https://doi.org/10.1016/j.sedgeo.2004.05.009

SUPPORTING INFORMATION

Additional supporting information can be found online in the Supporting Information section at the end of this article.

Dataset S1. Electron microprobe representative compositions of major and accessory minerals from the rutile-bearing ilmenitite (ACL-5-10B).

Figure S1. Chemistry of högbomite from the CMC. (a) Chemical composition of studied högbomite compared with occurrences in metamorphic rocks and other Ti-Fe ore deposits associated with anorthosites. (b-e) Compositional profile along a texture of högbomite replacing spinel. (f-j) Chemical differences between prismatic högbomite and högbomite formed after spinel.

Figure S2. X-ray diffraction data from rutile-bearing ilmenitite showing peaks for clinochlore chlorite.

Figure S3. ZrO_2, HfO_2, and Cr_2O_3 compositional profiles across a single coarse-grained rutile.

Figure S4. Hydrothermal vs magmatic discrimination of zircon based on trace element concentrations after Hoskin (2005).

Figure S5. Location of analyses for Zr-in-rutile thermometry over different rutile textures.

Figure S6. Zircon crystals in anorthosite micro-inclusions in oxide-apatite-rich amphibolite showing association to former Ti-Fe oxide minerals now transformed to titanite.

Figure S7. Isothermal Zr-in-rutile diffusion modelling from grains associated to zircon and högbomite employing the Zr diffusion coefficient from Cherniak et al.

(2007). Lines of different colour represent distinct timescales applied to the model.

Table S1. Electron microprobe compositional profiles in the rutile-bearing ilmenitite (ACL-5-10B).

Table S2. Integrated age, oxygen isotopes, and trace element compositions from zircon of the rutile-bearing ilmenitite (ACL-5-10B).

Table S3. Oxygen isotope compositions from zircon from the rutile-bearing ilmenitite sample (ACL-5-10B).

Table S4. Zr concentrations and Zr-in-rutile temperatures of texturally different rutile crystals from the rutile-bearing ilmenitite sample ACL-5-10B.

Table S5. Pb-corrected U–Pb ages for zircon from anorthosite (CH17-1), rutile-bearing ilmenitite (ACL-5-10B), and oxide-apatite-rich amphibolite (NF1302).

Table S6. Common Pb-uncorrected U–Pb ages for zircon separates from rutile-bearing ilmenitite sample (ACL-5-10B).

Table S7. Common Pb-uncorrected in-situ U–Pb baddeleyite dating from the rutile-bearing ilmenitite sample ACL-5-10B.

Table S8. Common Pb-uncorrected in-situ U–Pb rutile ages from rutile-bearing ilmenitite (ACL-5-10B) and anorthosite (ENFORT-01).

How to cite this article: Cisneros de León, A., Schmitt, A. K., & Weber, B. (2022). Multi-episodic formation of baddeleyite and zircon in polymetamorphic anorthosite and rutile-bearing ilmenitite from the Chiapas Massif Complex, Mexico. *Journal of Metamorphic Geology*, *40*(9), 1493–1527. https://doi.org/10.1111/jmg.12683